Oil & Natural Gas Technology

Detection and Production of Methane Hydrate

Semi-annual Progress Report

Reporting Period: May -October, 2009

Submitted by:
Rice University, University of Texas, and Oklahoma State University

George J. Hirasaki and Walter Chapman, Chemical and Biomolecular Engineering
Gerald R. Dickens, Colin A. Zelt, and Brandon E. Dugan, Earth Science
Kishore K. Mohanty, University of Texas
Priyank Jaiswal, Oklahoma State University

November, 2009

DOE Award No.: DE-FC26-06NT42960
John Terneus, Program Officer

Rice University – MS 362
6100 Main St.
Houston, TX 77251-1892
Phone: 713-348-5416; FAX: 713-348-5478; Email: gjh@rice.edu

Prepared for:
United States Department of Energy
National Energy Technology Laboratory

Office of Fossil Energy

Table of Contents

Disclaimer

Executive Summary

Task 5: Carbon Inputs and Outputs to Gas Hydrate Systems

The abundance and distribution of gas hydrate in marine sediment sequences depend on inputs and outputs of carbon over time. The primary input is solid organic carbon, which is converted to methane. The primary outputs for many systems are anaerobic oxidation of methane and gas burial. The primary scope of this task is to generate chemical constraints on carbon inputs and outputs, which can be incorporated into numerical models. We have generated all data, we are presenting and writing the results, and we are incorporating the results into models.

Task 6: Numerical Models for Quantification of Hydrate and Free Gas Accumulations

Subtask 6.3 *Compositional Effect on BSR.* Code is being developed to compute the hydrocarbon composition as well as hydrate and free gas saturations when multiple hydrocarbon components are transported in marine sediments. Also seismic code to generate synthetic seismic profiles is being tested.

Subtask 6.8 (b): Sulfate, Bicarbonate, Calcium and carbon isotope ($\delta^{13}C$) balance as an indicator of methane flux. Code has been developed to model the contrasting mechanisms proposed by Dickens and by Kastner. We will try to resolve the conditions for validity of each interpretation.

Task 7: Analysis of Production Strategy

Water and gas relative permeability curves were computed as a function of hydrate saturation using a pore structure model.

Task 8: Seafloor and Borehole Stability

We primarily focused on modeling of sediment instability associated with hydrate accumulations (Subtask 8.2) that builds on our work of sediment-hydrate properties (Subtask 8.1) because the models use these properties as inputs. We are continually extending our collaborations and data integration (Subtask 8.3) as we test the instability models against field data collected by DOE, IODP, and other international programs.

Task 9: Geophysical Imaging of Gas Hydrate and Free Gas Accumulations

We have made the first estimates of hydrate quantities along the seismic profile (Subtask 9.3) using results from our processing and modeling exercise (Subtask 9.1). Subtask 9.2 (waveform inversion) has been put to a halt after an initial attempt in July 2009 as I am trying to build my computational lab at Oklahoma State University to the same specifications as at Rice University. I expect to resume Subtask 9.2 from January.

Background

A. Objective

This project seeks to understand regional differences in gas hydrate systems from the perspective of as an energy resource, geohazard, and long-term climate influence. Specifically, the effort will: (1) collect data and conceptual models that targets causes of gas hydrate variance, (2) construct numerical models that explain and predict regional-scale gas hydrate differences in 2- and 3-dimensions with minimal "free parameters", (3) simulate hydrocarbon production from various gas hydrate systems to establish promising resource characteristics, (4) perturb different gas hydrate systems to assess potential impacts of hot fluids on seafloor stability and well stability, and (5) develop geophysical approaches that enable remote quantification of gas hydrate heterogeneities so that they can be characterized with minimal costly drilling. Our integrated program takes advantage of the fact that we have a close working team comprised of experts in distinct disciplines.

The expected outcomes of this project are improved exploration and production technology for production of natural gas from methane hydrates and improved safety through understanding of seafloor and well bore stability in the presence of hydrates.

B. Scope of Work

The scope of this project is to more fully characterize, understand, and appreciate fundamental differences in the amount and distribution of gas hydrate and how this affects the production potential of a hydrate accumulation in the marine environment. The effort will combine existing information from locations in the ocean that are dominated by low permeability sediments with small amounts of high permeability sediments, one permafrost location where extensive hydrates exist in reservoir quality rocks and other locations deemed by mutual agreement of DOE and Rice to be appropriate. The initial ocean locations are Blake Ridge, Hydrate Ridge, Peru Margin and GOM. The permafrost location is Mallik. Although the ultimate goal of the project is to understand processes that control production potential of hydrates in marine settings, Mallik will be included because of the extensive data collected in a producible hydrate accumulation. To date, such a location has not been studied in the oceanic environment. The project will work closely with ongoing projects (e.g. GOM JIP and offshore India) that are actively investigating potentially economic hydrate accumulations in marine settings.

The overall approach is fivefold: (1) collect key data concerning hydrocarbon fluxes which is currently missing at all locations to be included in the study, (2) use this and existing data to build numerical models that can explain gas hydrate variance at all four locations, (3) simulate how natural gas could be produced from each location with different production strategies, (4) collect new sediment property data at these locations that are required for constraining fluxes, production simulations and assessing sediment stability, and (5) develop a method for remotely quantifying heterogeneities in gas hydrate and free gas distributions. While we generally restrict our efforts to the locations where key parameters can be measured or constrained, our ultimate aim is to make our efforts universally applicable to any hydrate accumulation.

Task 5: Carbon Inputs and Outputs to Gas Hydrate Systems

Approach

The amount and distribution of gas hydrate in marine sediment depends on several factors. Our project-related modeling efforts (Bhatnager et al., 2007a, 2008), as well as results from other studies (e.g., Davie and Buffett, 2001; Garg et al., 2008), show that two particularly important factors are: (1) the flux of labile organic carbon over time, and (2) loss of methane via anaerobic oxidation of methane (AOM). We are trying to constrain these factors by generating key chemical data sets using sediment obtained from present-day gas hydrate systems.

Results and Discussion

We have generated a series of iodine profiles for sediment and pore waters through several gas hydrate systems (Blake Ridge, Peru Margin, Gulf of Mexico, Japan Sea). The profiles at Blake Ridge and Peru Margin have a fairly straightforward interpretation. Organic carbon lands on the seafloor with iodine. During burial, iodine is released from the organic carbon, contributing to iodide in pore water. This iodide moves upward toward the seafloor, by diffusion, advection or both. Here, it is converted to iodate and re-scavenged by organic carbon. The consequence is a system where the amount of iodine in pore waters is proportional to carbon input and fluid dynamics over time. This information can be used in our models. The iodine in the GOM and Japan Sea is not so easy to understand because, so far, it appears that there are external sources of iodine.

We are on the third draft of an iodine paper, which should have been submitted in the summer of 2009, but has been delayed. We are, however, making good progress at incorporating carbon and iodine into our models for gas hydrate formation. The overall idea here is that organic carbon added to the sediment sequence should give a specific gas hydrate profile as well as dissolved inorganic carbon and iodine profiles. We have also included sulfate and calcium into these models. We have submitted an abstract and will present the results at the Fall 2009 AGU Meeting (Chatergee et al., 2009).

We have generated a series of pore water and sediment data (metals and carbonate) across the sulfate-methane transition at sites with gas hydrate in the Japan Sea and on the Peru Margin. For all sites, there is an obvious sulfate-methane transition (SMT) with high amounts of authigenic carbonate (calcite) and barite. We interpret the SMT at these sites (and at most other gas hydrate locations) as resulting from AOM, and the authigenic mineral fronts as reflecting methane output that has been similar to present-day over a long time (>100,000 years) interval (i.e., steady-state). The results of the Japan Sea have been published (Snyder et al., 2007). The results from the Peru Margin should have been published this summer, but have been delayed. However, we did present the results at the International Workshop on the Biogeochemistry of Cold Seeps in September, 2009 (Dickens and Snyder, 2009a).

Our interpretations of processes across the SMT contrast with those of some authors. Specifically, we believe that the depth of the SMT is directly related to the loss of methane whereas some authors suggest it results from oxidation of organic carbon. We wrote a short article explaining our views and why we think the alternative interpretation is incorrect (Dickens and Snyder, 2009).

We have now calculated sulfate and bicarbonate fluxes at 22 “gas hydrate” sites at 7 locations. These locations span a range of parameters (e.g., water depth, SMT depth, etc.). So far, most data supports our interpretations and assumptions that methane flux can be calculated from sulfate profiles. We were in the middle of writing a summary paper on this topic, but encountered some discrepancies and thought to understand these first. One problem we have now found is that pore water data from Cascadia Margin sites have been reported incorrectly because of the top of sediment is missing in some holes (i.e., the reported SMT is too shallow). Another problem is that there are significant drops in porosity across authigenic horizons at some locations.

We have collected and analyzed samples from a location on the Peru Margin for carbon isotopes. The authigenic carbonates have a d13C of -6 per mil, even though we believe they are the result of AOM. This is because, in our opinion, there is a major upward flux of bicarbonate enriched in ^{13}C. We are now including carbon isotopes in our modeling.

While tangentially related to this project, we have now submitted a paper to Nature Geoscience concerning the long-term effect of temperature on gas hydrate abundance (Guangsheng Gu et al., submitted). Essentially, we have used our model, with our chemical constraints, to understand in gas hydrate amounts under different seafloor temperature. Contrary to most intuition, warmer water can hold more gas hydrate at certain water depths because of increased methanogenesis at higher temperatures.

Conclusions

Models concerning the abundance and distribution of gas hydrate in marine sediment require constraints on carbon inputs and outputs, fluid flow and temporal evolution. Our chemical analyses of sediment appear to be providing us interesting constraints that we can use in our models.

Task 6: Numerical Models for Quantification of Hydrate and Free Gas Accumulations

Subtask 6.3. Compositional Effect on BSR: Guangsheng Gu

From the work we have finished, we have found that existence of another gas component in marine hydrate system can affect the hydrate and gas distribution greatly. As an example, in a CH_4-C_3H_8-H_2O hydrate system, there can exist a transition region in which *Aq*, *H* (sII) and *V* can co-exist, and S_H and S_v can change gradually. The transition zone can be as thick as 300 m. The p-wave velocity V_p, may vary gradually throughout this transition zone, and induce a weak or even unobservable BSR. From synthetic seismic responses, weak BSR or very weak BSR is possible if λ_c/L_{stz} <1, where λ_c is the characteristic wavelength, and L_{stz} is the transition zone thickness. Our results suggest that, for a multiple gas system, it's better to use multiple frequencies to detect BSR, and most important, to use low frequencies to observe transition zones due to compositional effects. These results are encouraging for further simulation. A manuscript on compositional effect based on these preliminary results is in progress and will be finished in this month.

We are trying to develop a code to simulate the compositional effects under seafloor. There are two important but challenging steps:

(1) Do flash calculation for a 4-phase, 3-component system. 4 phases include: Gas (or Vapor, *G* or *V*), Aqueous (*Aq*), Hydrate structure I (s*I*), Hydrate structure II (s*II*). In some cases, we know that there are only 3 phases, so it can be reduced to a 3-phase system. However, sometimes a liquid hydratcarbon (Liquid, *L*), may be involved, and it'll be a 5-phase system. 3 components include: water, methane, and another heavier gas component (e.g., propane, ethane, or CO_2, *etc*.).

(2) A diffusion and convection model for multi-phase and multi-component systems. The transport model will include diffusion and convection of methane, and another heavier gas component, within one phase or among different phases. Different geothermal gradient and pressure distribution will be considered.

Since the multi-phase, multi-component flash calculation is challenging but important in this work, we are trying to apply some good flash calculation model and algorithms.

Flash calculation model

In a F-phase, C-component system, use phase *F* as the reference phase. In equilibrium we have:

$$y_{ij}\hat{\varphi}_{ij} = y_{iF}\hat{\varphi}_{iF} \quad , i=1,2,\ldots, C; j=1,2,\ldots,F-1 \qquad (1)$$

y_{ij} --- composition of component *i*, in phase *j*

$\hat{\varphi}_{ij}$ --- fugacity coefficients of component *i*, in phase *j*

The material balance equation for component *i* is:

$$\sum_{j=1}^{F} \beta_j y_{ij} = z_i, \; i=1,2,\ldots,C \qquad (2)$$

β_j --- mole fraction of phase *j* with respect to overall material amount

z_i --- overall material amount of component *i* in the system

The mole fractions β_j satisfy a normalization property:

$$\sum_{j=1}^{F} \beta_j = 1$$

or:

$$\beta_F = 1 - \sum_{j=1}^{F-1} \beta_j \qquad (3)$$

Substitute Eq. 3 into Eq. 2, we have the material balance as:

$$y_{iF} + \sum_{j=1}^{F-1} \beta_j (y_{ij} - y_{iF}) = z_i \qquad (4)$$

Define K-factor:

$$K_{ij} = y_{ij} / y_{iF} = \hat{\varphi}_{iF} / \hat{\varphi}_{ij} \qquad (5)$$

Substitute Eq.5 into Eq.3:

$$y_{iF}\left(1 + \sum_{l=1}^{F-1} \beta_l (K_{il} - 1)\right) = z_i \qquad (6)$$

or :

$$y_{iF} = \frac{z_i}{1 + \sum_{l=1}^{F-1} \beta_l (K_{il} - 1)} \qquad (7)$$

and

$$y_{ij} = \frac{z_i K_{ij}}{1 + \sum_{l=1}^{F-1} \beta_l (K_{il} - 1)} \qquad (8)$$

From Eq.3~ Eq.8, we can obtain *F*-1 equations with *F*-1 unknown, β_j, as:

$$\sum_{i=1}^{C} \frac{K_{ij} - 1}{1 + \sum_{l=1}^{F-1} \beta_l (K_{il} - 1)} = 0, \text{ j=1,2,…,F-1} \qquad (9)$$

From properties of phases and components, fugacity coefficients, K_{ij} can be obtained from Eq.5; then, phase fractions β_j can be estimated by solving Equation set 9; finally, phase compositions y_{ij}, will be easily obtained from Eq.7 and Eq.8.

Normally, Equation set 9 can be solved by Newton method. However, many situations happen at which adjustments are required. For example, phase fraction β_j may be negative or greater than 1. So some constraints should be applied as:

$$1 \geq \beta_j \geq 0\ ,\ j=1,2,\ldots,F-1 \qquad (10)$$

Equation set 9 also may be difficult to converge.

To solve Equation set 9, a better method is as following.

Define an objective function

$$Q(\beta) = \sum_{j=1}^{F} \beta_j - \sum_{i=1}^{C} z_i \ln E_i \ , \qquad (11)$$

where $$E_i = \sum_{k=1}^{F} \left(\beta_k / \hat{\varphi}_{ik} \right), \qquad (12).$$

It can be proved that in this case, a solution β_j will minimize Q while subjecting to Eq.14-15. So the problem becomes an optimization problem:

$$\min_{\beta \in R^F} Q(\beta) \qquad (13)$$

subject to: $\beta_j \geq 0,\ j=1,2,\ldots,F \qquad (14)$

$$\sum_{j=1}^{F} \beta_j = 1 \qquad (15)$$

The solution is given by

$$\begin{cases} \dfrac{\partial Q}{\partial \beta_j} = 0 \quad : \quad \beta_j > 0 \\ \dfrac{\partial Q}{\partial \beta_j} > 0 \quad : \quad \beta_j = 0 \end{cases} \qquad (16)$$

The gradient of $\mathcal{L}$ is

$$g_j = \frac{\partial Q}{\partial \beta_j} = 1 - \sum_{i=1}^{C} \frac{z_i}{E_i} \frac{1}{\hat{\varphi}_{ij}} \qquad (17)$$

At solution, the mole fraction can be calculated by:

$$y_{ij} = \frac{z_i}{E_i} \frac{1}{\hat{\varphi}_{ij}} \qquad (18)$$

Numerical code for a 4-phase, 3-component system is in progress now. More results may be available in next season.

Synthetic seismic response

To better understand seismic features in many fields, it's necessary to simulate the seismic response by ourselves. Once we obtained the hydrate distribution, we can estimated the V_p distribution, and then by means of available seismic modeling code, it's possible to generate synthetic seismic response. By comparing the synthetic seismic response with available field data, we may understand what's going on and explain some seismic phenomena such as weak BSR and amplitude blanking. Another reason I started work on this code is that Dr. Priyank Jaiswal has left Houston to Oklahoma State University, I need to carry out more work on seismic response simulation.

I started practicing codes to generate synthetic seismic response in summer. The code is a 2D waveform inversion code by Prof. Gerhard Pratt (1999). What's more, I attended a summer school on seismic imaging, in University of Washington, in August. By using the waveform inversion code, for simple velocity models, we can generate good seismic responses. For example, a simple situation is a system with a BSR below seafloor as below.

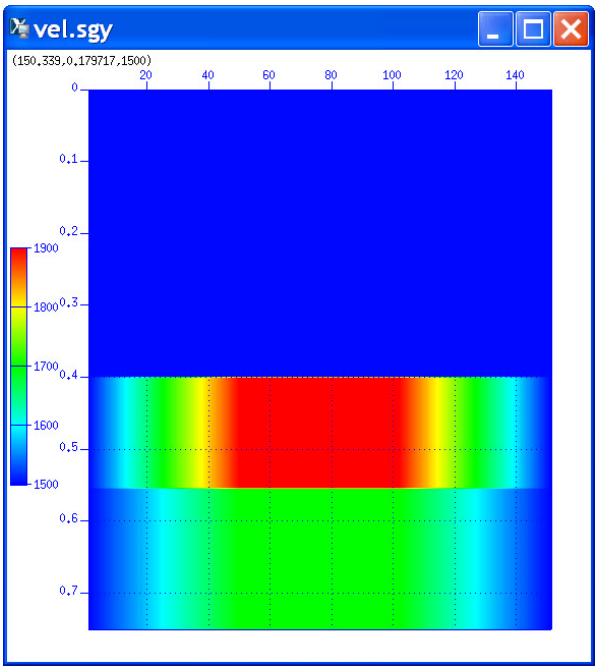

Figure 1. V_p distribution for the code

Vertical axis (Depth): km; Lateral axis: m. *Vp* value: m/s. The 1st reflector is seafloor; the 2nd reflector is assumed to be a BSR.

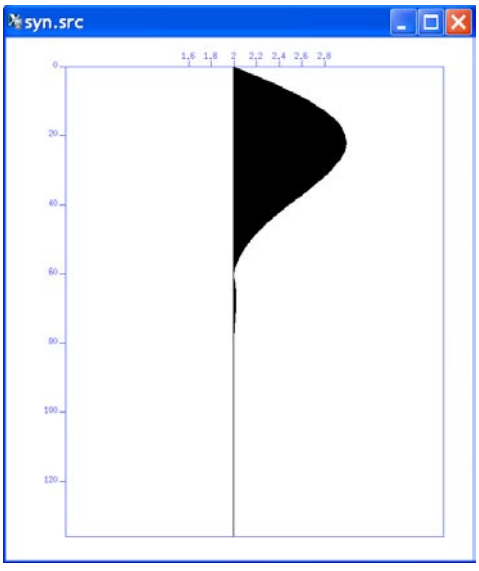

(a)

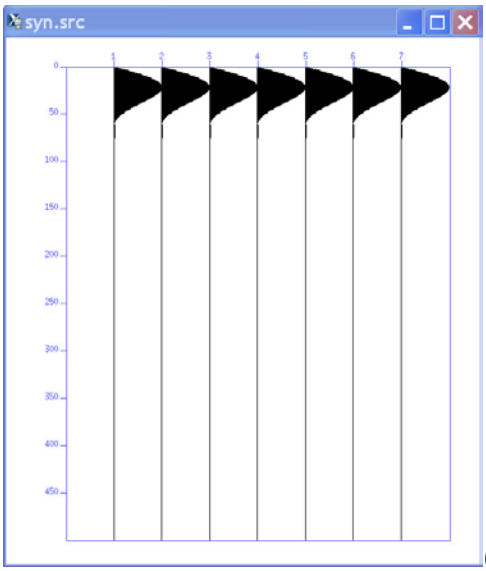

(b)

Figure 2. Source wavelet (Ricker Wavelet) in frequency domain
Horizontal axis: amplitude; vertical axis: frequency.
(a) A single source wavelet; (b) Positions of 7 sources, generating same wavelets simultaneously.

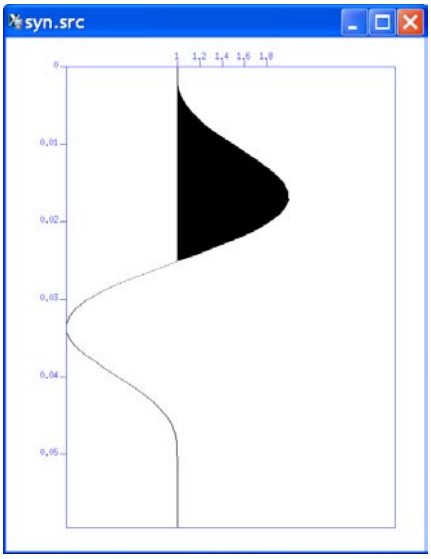

(a)
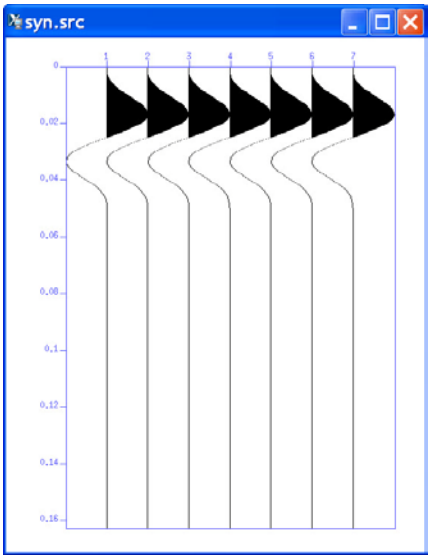

(b)

Figure 3. Source wavelet in time domain
Horizontal axis: amplitude; vertical axis: time (sec).
(a) A single source wavelet; (b) Positions of 7 sources, generating same wavelets simultaneously.

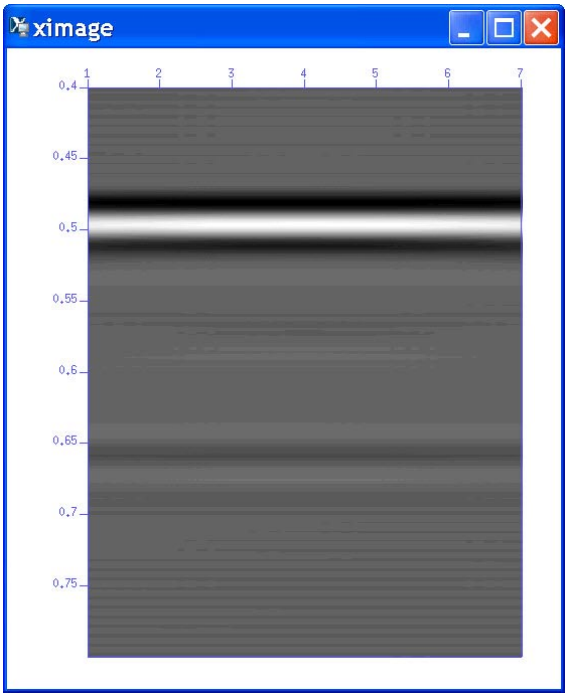

Figure 4. Synthetic Seismic Response

Horizontal axis: lateral position (unit is 10m); vertical axis: two-way-travel-time (sec). A strong BSR-type response is clearly shown here.
Notice: The response from the 1st reflector (seafloor) is not shown because it's too strong.

In the future we are going to use this code to simulate seismic response from more complex hydrate distributions.

Presentations

1. Massive Methane Hydrate in Sediments to Cause the Paleocene/Eocene Thermal Maximum. Guangsheng Gu, Gerald R. Dickens, Gaurav Bhatnagar, Frederick S. Colwell, Walter Chapman, George J. Hirasaki*, AGU Fall meeting, 2009, San Francisco, Dec. 14-18.

Massive Methane Hydrate in Sediments to Cause the Paleocene/Eocene Thermal Maximum

Guangsheng Gu[1], Gerald R. Dickens[2], Gaurav Bhatnagar[1$], Frederick S. Colwell[3], Walter Chapman[1], George J. Hirasaki[1*]

Abstract: During the Paleocene/Eocene thermal maximum (PETM) about 55 million years ago (Ma) through the end of the early Eocene climatic optimum about 49 Ma, the carbon isotope ratio, $\delta^{13}C$, in the deep ocean, decreased by ~2.5‰ within a very short period. This corresponded to a rapid massive injection of ^{13}C-depleted carbon into the oceanic system. Many mechanisms for this carbon injection have been proposed, among which the release of ^{13}C-depleted methane from gas hydrate due to thermal dissociation has received considerable support. However, one issue with this hypothesis still remains: the ocean bottom waters were 10°C warmer in the latest Paleocene than today, which implies a smaller global volume of sediment hosting gas hydrate. Here we present results from a numerical model for gas hydrate accumulation in marine sediment where all critical parameters are adjusted to higher bottom water temperature. We assume, at a higher seafloor temperature than today: the oxygen concentration in ocean was lower, therefore the amount of organic carbon depositing on sediment was higher; and so was the methanogenesis rate constant in sediment. The results show that, at a higher seafloor temperature as in the late Paleocene than today, depending on water depth and initial conditions regarding organic carbon inputs, gas hydrate abundance was lower in some marine sediment columns but higher in others. This counterintuitive result reflects greater organic carbon input with lower dissolved oxygen and faster methanogenesis at higher temperatures during PETM.

1 Department of Chemical and Biomolecular Engineering, Rice University, Houston, TX 77005, USA.
2 Department of Earth Science, Rice University, Houston, Texas, 77005, USA.
3 College of Oceanic and Atmospheric Sciences, Oregon State University, Corvallis, OR, 97331, USA
* Corresponding author: George J Hirasaki (gjh@rice.edu)
$. Currently in Shell Co. Ltd.

Manuscripts

1. Elevated Ocean Bottom Water Temperature and Abundant Marine Gas Hydrate in the Early Palaeogene. Guangsheng Gu, Gerald R. Dickens*, Gaurav Bhatnagar, Frederick S. Colwell, George J. Hirasaki, Walter Chapman. Submitted.

2. Compositional Effect on Hydrate/Free Gas Transition and BSR. In progress, to be submitted in November.

Academic Activities Attended

1. Summer school on seismic imaging, University of Washington, Seatle, WA. Aug. 10-14, 2009.

2. Society of Exploration Geophysicists 2009 Annual Meeting, Houston, TX, Oct. 25-30, 2009.

Subtask: Case studies--started

We have started case-study on K-G basin, results may be available in the following 2 months.

Task 6: Numerical Models for Quantification of Hydrate and Free Gas Accumulations

Subtask 6.8 (b): Sulfate, Bicarbonate, Calcium and carbon isotope ($\delta^{13}C$) balance as an indicator of methane flux**:** Sayantan Chatterjee

The upward flux of methane is an important constraint on the amount and distribution of gas hydrate that can occur in marine sediment. For diffusion dominated gas hydrate systems, one potential approach for determining this flux is to use the depth of the sulfate methane transition (SMT). Pore water sulfate concentrations drop to near zero values in shallow sediment above all marine gas hydrate systems. The depletion is generally underlain by a rapid increase in methane concentrations, such that a thin SMT occurs in the upper 30 or so meters of sediment. Many authors have attributed these chemical gradients to anaerobic oxidation of methane (AOM) at the SMT. Indeed, if AOM dominates consumption of methane and sulfate, and the system is at steady-state conditions, the depth of the SMT should be related directly to the upward flux of methane (e.g., Borowski *et al.*, 1996; Dickens and Snyder, 2007).

Presently, the use of sulfate profiles and the depth of SMT to calculate upward methane fluxes is controversial because various authors have interpreted pore water composition and carbon isotope data in shallow sediment differently, even at the same sites (e.g., Kastner et al., 2008; Dickens and Snyder, 2009). The roots of the problem are twofold: (1) sulfate consumption can occur through two reaction pathways, and (2) a reaction constituent, bicarbonate, has multiple sources and sinks. Other than AOM, Particulate Organic Carbon (POC) can remove sulfate form pore water.

The AOM reaction involves oxidation of one mole of methane and reduction of one mole of sulfate to produce one mole of bicarbonate and one mole of hydrogen sulfide:

$$CH_4 + SO_4^{2-} \rightarrow HCO_3^- + HS^- + H_2O$$

By contrast, the POC reaction involves oxidation of one mole of solid organic carbon and reduction of one mole of sulfate to produce two moles of bicarbonate and one mole of hydrogen sulfide:

$$2CH_2O + SO_4^{2-} \rightarrow 2HCO_3^- + H_2S$$

One might discriminate between these two reactions using the amounts of reactants and products because the first reaction has a HCO_3^- : SO_4^{2-} stoichiometry of 1:1, whereas the latter reaction has a stoichiometry of 2:1.

Several authors (e.g., Kastner et al., 2008) have attempted to discriminate between the two reactions using pore water concentration profiles. In particular,

arguments for the dominance of a reaction have been made using cross plots of change in excess alkalinity versus change in sulfate concentration (e.g., figure 6.8.1). Excess alkalinity is the amount of HCO_3^- that would occur in pore water if authigenic carbonate had not precipitated. The change in excess alkalinity can be computed by summing the deviations in pore water alkalinity, Ca^{2+} and Mg^{2+} relative to their respective concentration in seawater. The change in pore water sulfate concentration is relative to the seawater. In the case shown here (figure 6.8.1), there is a 2:1 slope, which might suggest that one mole of sulfate releases two moles of bicarbonate. If correct, this would support POC driven sulfate consumption (Kastner *et al*., 2008). Such an interpretation, however, is only valid for a closed system where sulfur and carbon fluxes in and out of sediment horizons are zero. This situation does not occur in most areas with gas hydrate because fluxes through diffusion are faster than through sedimentation.

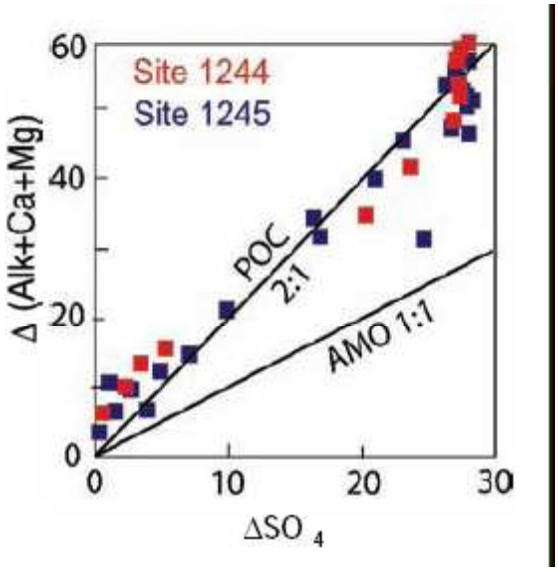

Figure 6.8.1: A cross plot of excess alkalinity corrected for carbonate precipitation versus SO_4^{2-}(mM) at two of the hydrate ridge sites 1244 and 1245 (Kastner *et al*., 2008)

An analysis of reactants and products using fluxes is a much better approach for understanding the stoichiometry of the sulfate consumption reaction. This is particularly true because there is often a flux of bicarbonate into the SMT from below (Dickens and Snyder, 2009). For example, at Site 1244, when one calculates fluxes of bicarbonate, there are −6mol/m^{2}kyr of HCO_3^- entering the SMT from below and −22mol/m^{2}kyr of HCO_3^- leaving the SMT towards the seafloor. This gives a net change of −16mol/m^{2}kyr of HCO_3^- across the SMT. This nicely balances the +16mol/m^{2}kyr of SO_4^{2-} entering the SMT, suggesting a 1:1 stoichiometry (Dickens and Snyder, 2009).

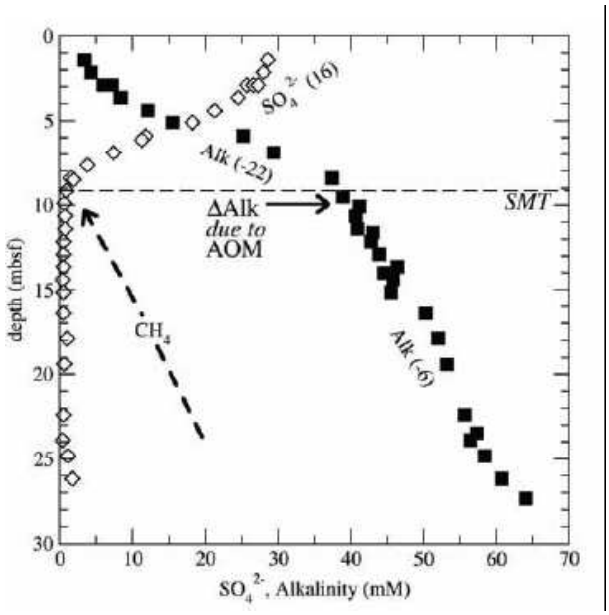

Figure 6.8.2: Pore water data in shallow sediment at ODP 1244, Hydrate Ridge (Trehu *et al*., 2003). Also shown are the SMT, estimated fluxes of dissolved species (mol/m^{2}kyr) in and out of the SMT (Dickens and Snyder, 2009)

The source of deep flux of bicarbonate is from the biogenic generation of methane that takes place in deeper sediments. The methanogenesis reaction involves breakdown of two moles of particulate organic carbon to form one mole of methane and one mole of carbon dioxide under the action of archaebacteria via a series of reactions as shown below:

Fermentation:

$$6CH_2O + 2H_2O \rightarrow 2CH_3COOH + 2CO_2 + 4H_2$$

Methanogenesis:

$$CO_2 + 4H_2 \rightarrow CH_4 + 2H_2O$$

$$2CH_3COOH \rightarrow 2CH_4 + 2CO_2$$

Overall Reaction:

$$2CH_2O \rightarrow CH_4 + CO_2$$

The carbon dioxide reacts with pore water to form bicarbonate.

$$CO_2 + H_2O \rightarrow HCO_3^- + H^+$$

Over geologic timescales, sedimentation and deposition of older sediments buries the organic carbon to greater depths. This gives rise to the deeper bicarbonate flux coming from below.

The carbon isotopic composition ($\delta^{13}C$) of dissolved inorganic carbon (DIC) across the SMT has also been used to infer the reaction path (e.g., Kastner et al., 2008). The overall idea is that POC has a $\delta^{13}C$ of -25‰ whereas biogenic methane has a $\delta^{13}C$ of -60‰, so the isotopic composition of DIC at the SMT should give the proportion generated from AOM and POC. For example, the nominally -25‰ of DIC across the SMT at Site 1244 has been argued to reflect a dominance of POC consumption of sulfate.

However, bicarbonate formed during methanogenesis typically has an isotopic composition of +10‰ or greater. This means that, in an open system, the measured $\delta^{13}C$ of bicarbonate across the SMT is the net result of $\delta^{13}C$ formed by reactions at the SMT (e.g., AOM) and bicarbonate fluxing in to and out of the SMT. A DIC of -25‰ across the SMT can result from AOM and a deep bicarbonate flux with a $\delta^{13}C$ of +10‰ or greater (Dickens and Snyder, 2009).

Proposed work: Numerical model with two reaction pathways for pore water sulfate consumption

Rate of Reaction Model

To reconcile the two interpretations regarding sulfate reduction stoichiometry and carbon isotope balance, we are extending our 1-D model (Bhatnagar et al., 2007, 2008) to include mass balances for sulfate consumption. The numerical model involves four primary chemical reactions involving different species. The first three reactions are listed below along with their corresponding kinetic models defining the kinetic rate of the respective chemical reactions. The fourth reaction is a reversible reaction and the equilibrium model is listed below.

Methanogenesis reaction

$$2CH_2O + H_2O \rightarrow CH_4 + HCO_3^- + H^+ \qquad r_{meth} = -\lambda\alpha$$

AOM reaction at the SMT

$$CH_4 + SO_4^{2-} \rightarrow HCO_3^- + HS^- + H_2O \qquad r_{AOM} = -\lambda_{AOM} c_m^l c_s^l$$

POC driven sulfate consumption

$$2CH_2O + SO_4^{2-} \rightarrow 2HCO_3^- + H_2S \qquad r_{POC} = -\lambda_{POC}\alpha c_s^l$$

Calcite precipitation reaction

$$HCO_3^- + Ca^{2+} \qquad H^+ + CaCO_3 \downarrow \qquad r_{ppt} = \frac{\Delta c_{CaCO_3}^l}{\Delta t}$$

The methanogenesis rate of reaction is given as λ. The rate of reaction for sulfate reduction by POC is given as λ_{POC}, and AOM reaction is given as λ_{AOM}. The calcite precipitation is a equilibrium reaction and the rate is given by the amount of calcium carbonate formed in a given time. Unlike the kinetic modeling for the other irreversible reactions, equilibrium rate for the calcite precipitation reaction is modeled differently as a function of formation of calcium carbonate. The phase concentration for the different species are represented as C_m^l for Methane, C_s^l for Sulfate, C_t^l for Bicarbonate, C_{cc}^l for Calcium, $c_{CaCO_3}^l$ for Calcium Carbonate and α for particulate organic carbon.

We assume that the hydrogen ions that are being formed in the system as a product of different reactions, at the same time being transported by convection and diffusion, thereby avoiding accumulation of hydrogen ions which would eventually make the formation acidic and the reactions would eventually stop. However, we will not be modeling the hydrogen ion transport in our current work.

Methane Mass Balance

Following previous work (Bhatnagar *et al.*, 2007), the methane mass balance equations have been simplified to exclude the gas hydrate and free gas phase terms. They also assume methane generation from particulate organic carbon (POC) and consumption via anaerobic oxidation of methane (AOM) reaction in the balance equation (Bhatnagar *et al*. 2008).

$$\frac{\partial}{\partial t}(\phi S_w \rho_w c_m^l) + \frac{\partial}{\partial z}(U_f \rho_w c_m^l) = \frac{\partial}{\partial z}(\phi \rho_w S_w D_m \frac{\partial c_m^l}{\partial z}) + \frac{M_{CH_4}}{M_{POC}} \rho_{sed}(1-\phi)\lambda\alpha$$

$$- \frac{\phi S_w \lambda_{AOM}(\rho_w c_m^l)(\rho_w c_s^l)}{M_{SO_4}}$$

Dimensionless Methane Mass Balance

The above equation can now be made dimensionless using the scaling scheme developed by Bhatnagar *et al*. (2007). The dimensionless mass balance equation is presented as follows.

$$\frac{\partial}{\partial \tilde{t}}\left[\frac{(1+\gamma\tilde{\phi})S_w \tilde{c}_m^l}{\gamma}\right] + \frac{1+\gamma}{\gamma}\frac{\partial}{\partial \tilde{z}}\left[(Pe_1 + |Pe_2|)\,\tilde{U}_f \tilde{c}_m^l\right]$$

$$= \frac{\partial}{\partial \tilde{z}} \left[\frac{(1+\gamma\tilde{\phi})S_w}{\gamma} \frac{\partial \tilde{c}_m^l}{\partial \tilde{z}} \right] + \frac{M_{CH_4}}{M_{POC}} \tilde{\rho}_{sed} Da (1-\tilde{\phi}) \tilde{\alpha} \beta$$

$$- \frac{(1+\gamma\tilde{\phi})S_w}{\gamma} \frac{M_{CH_4} c_{s,o}}{M_{SO_4} c_{m,eqb}^l} Da_{AOM} \tilde{c}_m^l \tilde{c}_s^l$$

The terms on the left are the accumulation term followed by the convection term. The terms on the right hand side represents diffusion, methane generation due to organic carbon input into the system and methane consumption due to sulfate reduction reaction via anaerobic oxidation of methane (AOM) from left to right.

Sulfate Mass Balance

The sulfate mass balance is in the water phase only and it includes both the reaction pathways for sulfate consumption. The anaerobic oxidation of methane and sulfate reduction by particulate organic carbon both act as sinks for pore water sulfate and both these reactions are included in the mass balance equations (Bhatnagar *et al*. 2008).

$$\frac{\partial}{\partial t}(\phi S_w \rho_w c_s^l) + \frac{\partial}{\partial z}(U_f \rho_w c_s^l) = \frac{\partial}{\partial z}(\phi \rho_w S_w D_s \frac{\partial c_s^l}{\partial z}) - \frac{\phi(1-\phi)S_w}{M_{POC}} \lambda_{POC} (\rho_{sed} \alpha)(\rho_w c_s^l)$$

$$- \frac{\phi S_w \lambda_{AOM} (\rho_w c_m^l)(\rho_w c_s^l)}{M_{CH_4}}$$

Dimensionless Sulfate Mass Balance

$$\frac{\partial}{\partial \tilde{t}} \left[\frac{(1+\gamma\tilde{\phi})S_w \tilde{c}_s^l}{\gamma} \right] + \frac{1+\gamma}{\gamma} \frac{\partial}{\partial \tilde{z}} \left[(Pe_1 + |Pe_2|) \tilde{U}_f \tilde{c}_s^l \right]$$

$$= \frac{\partial}{\partial \tilde{z}} \left[\frac{(1+\gamma\tilde{\phi})S_w}{\gamma} \frac{D_s}{D_m} \frac{\partial \tilde{c}_s^l}{\partial \tilde{z}} \right] - \frac{(1+\gamma\tilde{\phi})(1-\tilde{\phi})}{1+\gamma} \frac{D_s}{D_m} S_w \tilde{\rho}_{sed} Da_{POC} \beta \tilde{\alpha} \tilde{c}_s^l$$

$$- \frac{(1+\gamma\tilde{\phi})S_w Da_{AOM} \tilde{c}_m^l \tilde{c}_s^l}{\gamma}$$

The terms on the left are the accumulation term followed by the convection term. The terms on the right hand side represent diffusion, sulfate consumption due to organic carbon input (POC) into the system and sulfate consumption due to via anaerobic oxidation of methane (AOM) from left to right.

Bicarbonate Mass Balance

As pointed out previously, bicarbonate balance is a necessary step to investigate the competing hypotheses for the loss of sulfate. Similar to the sulfate balance, bicarbonate mass balance not only includes source terms originating from both AOM and POC reactions discussed above but also includes source terms like the methanogenesis reaction. The bicarbonate mass balance also includes a sink term corresponding to the calcite precipitation reaction as shown below.

$$\frac{\partial}{\partial t}(\phi S_w \rho_w c_b^l) + \frac{\partial}{\partial z}(U_f \rho_w c_b^l) = \frac{\partial}{\partial z}(\phi \rho_w S_w D_b \frac{\partial c_b^l}{\partial z}) + \frac{M_{HCO_3}}{M_{POC}} \rho_{sed}(1-\phi)\lambda\alpha$$

$$+\frac{2M_{HCO_3}\phi(1-\phi)S_w}{M_{POC}M_{SO_4}}\lambda_{POC}(\rho_{sed}\alpha)(\rho_w c_s^l) + \frac{M_{HCO_3}\phi S_w \lambda_{AOM}(\rho_w c_m^l)(\rho_w c_s^l)}{M_{CH_4}M_{SO_4}}$$

$$-\phi S_w \rho_w \frac{\partial c_{CaCO_3}^l}{\partial t}$$

The sink term originates from the calcium carbonate that precipitates in the reaction. When bicarbonate (or carbonate) and calcium react following a 1:1 stoichiometry, both the species continue to get consumed and forms calcium carbonate which precipitates out of solution as long as the product of calcium and bicarbonate concentration is greater than the solubility product (k_{sp}) of calcium carbonate. When the product of bicarbonate and carbonate concentrations equal the solubility product, their concentrations don't reduce any further, instead forms and precipitates an equivalent amount of calcium carbonate and the reaction reaches equilibrium. We model the equilibrium reaction in such a way that calcium concentration is constrained at the equilibrium concentration. Any calcium which gets consumed in excess of the equilibrium concentration forms calcium carbonate. Bicarbonate also gets reduced by a similar amount in the reaction over a particular time step. From the mass balance equations, we are able to compute the amount of calcium carbonate that forms during each time step after the convective and diffusive fluxes are computed**.**

Dimensionless Bicarbonate Mass Balance

$$\frac{\partial}{\partial\tilde{t}}\left[\frac{(1+\gamma\tilde{\phi})S_w\tilde{c}_b^l}{\gamma}\right]+\frac{1+\gamma}{\gamma}\frac{\partial}{\partial\tilde{z}}\left[(Pe_1+|Pe_2|)\,\tilde{U}_f\tilde{c}_b^l\right]=\frac{\partial}{\partial\tilde{z}}\left[\frac{(1+\gamma\tilde{\phi})S_w}{\gamma}\frac{D_b}{D_m}\frac{\partial\tilde{c}_b^l}{\partial\tilde{z}}\right]$$

$$+\frac{M_{HCO_3}c_{m,eqb}^l}{M_{POC}c_{b,o}}\tilde{\rho}_{sed}Da(1-\tilde{\phi})\tilde{\alpha}\beta+\frac{2M_{HCO_3}c_{s,o}S_w}{M_{SO_4}c_{b,o}}\frac{(1+\gamma\tilde{\phi})(1-\tilde{\phi})}{1+\gamma}\frac{D_s}{D_m}\tilde{\rho}_{sed}Da_{POC}\beta\tilde{\alpha}\tilde{c}_s^l$$

$$+\frac{1+\gamma\tilde{\phi}}{\gamma}\frac{M_{HCO_3}c_{s,o}}{M_{SO_4}c_{b,o}}S_wDa_{AOM}\tilde{c}_m^l\tilde{c}_s^l-\frac{(1+\gamma\tilde{\phi})}{\gamma}\frac{C_{Ca,o}}{C_{b,o}}S_w\frac{\partial\tilde{c}_{CaCO_3}^l}{\partial\tilde{t}}$$

The terms on the left are the accumulation term followed by the convection term. The terms on the right hand side represent diffusion, bicarbonate generation due to organic carbon input into the system, POC–sulfate reaction, anaerobic oxidation of methane reaction and bicarbonate consumption due to calcite precipitation from left to right.

Calcium Mass Balance

Calcium balance is also an important component in this model. The calcium mass balance includes the sink term corresponding to the calcite precipitation reaction and is presented below. The sink term is represented as the amount of calcium carbonate actually formed in the reaction.

$$\frac{\partial}{\partial t}(\phi S_w\rho_w c_{Ca}^l)+\frac{\partial}{\partial z}(U_f\rho_w c_{Ca}^l)=\frac{\partial}{\partial z}(\phi\rho_w S_wD_{Ca}\frac{\partial c_{Ca}^l}{\partial z})-\phi S_w\rho_w\frac{\partial c_{CaCO_3}^l}{\partial t}$$

Dimensionless Calcium Mass Balance

$$\frac{\partial}{\partial\tilde{t}}\left[\frac{(1+\gamma\tilde{\phi})S_w\tilde{c}_{Ca}^l}{\gamma}\right]+\frac{1+\gamma}{\gamma}\frac{\partial}{\partial\tilde{z}}\left[(Pe_1+|Pe_2|)\,\tilde{U}_f\tilde{c}_{Ca}^l\right]$$

$$=\frac{\partial}{\partial\tilde{z}}\left[\frac{(1+\gamma\tilde{\phi})S_w}{\gamma}\frac{D_{Ca}}{D_m}\frac{\partial\tilde{c}_{Ca}^l}{\partial\tilde{z}}\right]-\frac{(1+\gamma\tilde{\phi})}{\gamma}S_w\frac{\partial\tilde{c}_{CaCO_3}^l}{\partial\tilde{t}}$$

Carbon Isotope Mass Balance

We also include a carbon isotope mass balance in our current model. A simple carbon mass balance along with its isotopic composition for the different species provides an overall conservation of carbon isotopes in the system. In a previous section, it has been found that methane and bicarbonate are the two carbon species with different carbon isotopic composition for different reactions. This motivates us to write the carbon isotopic mass balance for methane and bicarbonate due to all the reactions sources and sinks in the system.

Carbon Isotope in Methane

$$\frac{\partial}{\partial t}(\phi S_w \rho_w c_m^l \delta_{CH_4}^{13}) + \frac{\partial}{\partial z}(U_f \rho_w c_m^l \delta_{CH_4}^{13}) = \frac{\partial}{\partial z}\left(\phi \rho_w S_w D_m \frac{\partial(c_m^l \delta_{CH_4}^{13})}{\partial z}\right)$$

$$+\frac{M_{CH_4}}{M_{POC}}\rho_{sed}(1-\phi)\lambda\alpha\delta_{CH_4,meth}^{13} - \frac{\phi S_w \lambda_{AOM}(\rho_w c_m^l)(\rho_w c_s^l)}{M_{SO_4}}\delta_{CH_4}^{13}$$

Dimensionless Carbon Isotope in Methane

$$\frac{\partial}{\partial \tilde{t}}\left[\frac{(1+\gamma\tilde{\phi})S_w \tilde{c}_m^l \delta_{CH_4}^{13}}{\gamma}\right] + \frac{1+\gamma}{\gamma}\frac{\partial}{\partial \tilde{z}}\left[(Pe_1 + |Pe_2|)\,\tilde{U}_f \tilde{c}_m^l \delta_{CH_4}^{13}\right]$$

$$= \frac{\partial}{\partial \tilde{z}}\left[\frac{(1+\gamma\tilde{\phi})S_w}{\gamma}\frac{\partial(\tilde{c}_m^l \delta_{CH_4}^{13})}{\partial \tilde{z}}\right] + \frac{M_{CH_4}}{M_{POC}}\tilde{\rho}_{sed} Da(1-\tilde{\phi})\tilde{\alpha}\beta\delta_{CH_4,meth}^{13}$$

$$-\frac{(1+\gamma\tilde{\phi})S_w}{\gamma}\frac{M_{CH_4}c_{s,o}}{M_{SO_4}c_{m,eqb}^l}Da_{AOM}\tilde{c}_m^l \tilde{c}_s^l \delta_{CH_4}^{13}$$

Carbon Isotope in Bicarbonate

$$\frac{\partial}{\partial t}(\phi S_w \rho_w c_b^l \delta_{HCO_3^-}^{13}) + \frac{\partial}{\partial z}(U_f \rho_w c_b^l \delta_{HCO_3^-}^{13}) = \frac{\partial}{\partial z}\left(\phi \rho_w S_w D_b \frac{\partial(c_b^l \delta_{HCO_3^-}^{13})}{\partial z}\right)$$

$$+\frac{M_{HCO_3}}{M_{POC}}\rho_{sed}(1-\phi)\lambda\alpha\delta_{HCO_3^-,meth}^{13} + \frac{2M_{HCO_3}\phi(1-\phi)S_w}{M_{POC}M_{SO_4}}\lambda_{POC}(\rho_{sed}\alpha)(\rho_w c_s^l)\delta_{HCO_3^-,POC}^{13}$$

$$+\frac{M_{HCO_3}\phi S_w \lambda_{AOM}(\rho_w c_m^l)(\rho_w c_s^l)}{M_{CH_4}M_{SO_4}}\delta_{CH_4}^{13} - \phi S_w \rho_w \frac{\partial}{\partial t}\left[c_{CaCO_3}^l \delta_{HCO_3^-}^{13}\right]$$

Dimensionless Carbon Isotope in Bicarbonate

$$\frac{\partial}{\partial \tilde{t}}\left[\frac{(1+\gamma\tilde{\phi})S_w\tilde{c}_b^l\delta^{13}_{HCO_3^-}}{\gamma}\right]+\frac{1+\gamma}{\gamma}\frac{\partial}{\partial\tilde{z}}\left[(Pe_1+|Pe_2|)\,\tilde{U}_f\tilde{c}_b^l\delta^{13}_{HCO_3^-}\right]$$

$$=\frac{\partial}{\partial\tilde{z}}\left[\frac{(1+\gamma\tilde{\phi})S_w}{\gamma}\frac{D_b}{D_m}\frac{\partial(\tilde{c}_b^l\delta^{13}_{HCO_3^-})}{\partial\tilde{z}}\right]+\frac{M_{HCO_3}c^l_{m,eqb}}{M_{POC}c_{b,o}}\tilde{\rho}_{sed}Da(1-\tilde{\phi})\tilde{\alpha}\beta\delta^{13}_{HCO_3^-,meth}$$

$$+\frac{2M_{HCO_3}c_{s,o}S_w}{M_{SO_4}c_{b,o}}\frac{(1+\gamma\tilde{\phi})(1-\tilde{\phi})}{1+\gamma}\frac{D_s}{D_m}\tilde{\rho}_{sed}Da_{POC}\beta\tilde{\alpha}\tilde{c}_s^l\delta^{13}_{HCO_3^-,POC}$$

$$+\frac{1+\gamma\tilde{\phi}}{\gamma}\frac{M_{HCO_3}c_{s,o}}{M_{SO_4}c_{b,o}}S_wDa_{AOM}\tilde{c}_m^l\tilde{c}_s^l\delta^{13}_{CH_4}-\frac{(1+\gamma\tilde{\phi})}{\gamma}\frac{C_{Ca,o}}{C_{b,o}}S_w\frac{\partial}{\partial\tilde{t}}\left[\tilde{c}^l_{CaCO_3}\delta^{13}_{HCO_3^-}\right]$$

where $\delta^{13}C_{CH4}$ corresponds to the $\delta^{13}C$ value in methane. The carbon isotope composition $\delta^{13}C$ value of methane during methanogenesis reaction due to biogenic sources corresponds to $\delta^{13}C_{CH4,\ meth}$. The carbon isotopic composition in methane during AOM reaction due to both the sources is represented as $\delta^{13}C_{CH4}$ since it is the current value of isotopic carbon being lost in the system at a particular time step. The $\delta^{13}C_{HCO3}$ denotes the $\delta^{13}C$ value in bicarbonate. The $\delta^{13}C$ value of bicarbonate during methanogenesis reaction is represented as $\delta^{13}C_{HCO3\ meth}$, and during POC reaction as $\delta^{13}C_{HCO3\ POC}$. During anaerobic oxidation of methane due to both the sources the isotopic carbon composition is $\delta^{13}C_{CH4}$ since it retains the same isotopic value as that in the methane, and during calcite precipitation reaction the value is the current value of $\delta^{13}C_{HCO3}$ at a specific time step. This summarizes all the mass balances required for the proposed numerical model.

The variable c_i correspond to concentration of phase *i* in the pore space, S_i to saturation of phase *i*, ρ_i to density of phase *i*, M_i to the molcular weight, and ϕ to porosity. The subscripts *m* correspond to methane, s correspond to Sulfate, *b* to Bicarbonate, *Ca* to calcium, $CaCO_3$ to Calcium Carbonate, *w* to water and *sed* to the sediment phase. The diffusivity of methane, sulfate, bicarbonate and calcium are represented by D_m, D_s, D_b, and D_{ca} respectively and the concentration of organic carbon input into the system is denoted by α. The molecular weights of different species methane, particulate organic carbon (POC), sulfate, bicarbonate, Calcium are denoted by M_{CH4}, M_{POC}, M_{SO4}, M_{HCO3}, and M_{ca} respectively. The vertical depth is normalized by the depth of the base of the gas hydrate stability zone (BHSZ) L_t, and is defined as $\tilde{z} = z/L_t$.

Time is normalized by a combination of L_t, depth of BHSZ and diffusivity of methane D_m and is represented as $\tilde{t} = \dfrac{t}{L_t^2 / D_m}$

We normalize the methane concentration $\tilde{c}_m^l$ with the equilibrium triple point methane solubility $\tilde{c}_{m,eqb}^l$ at the base of the hydrate stability zone (BHSZ) as $\tilde{c}_m^l = \dfrac{c_m^l}{\tilde{c}_{m,eqb}^l}$

We normalize the sulfate, bicarbonate and calcium concentration $\tilde{c}_s^l$, $\tilde{c}_b^l$, $\tilde{c}_{ca}^l$ with the seawater concentration value for sulfate (=30 mM) $\tilde{c}_{s,o}^l$, bicarbonate $\tilde{c}_{b,o}^l$(=2.29 mM) and calcium $\tilde{c}_{ca,o}^l$(=10 mM)

$$\tilde{c}_s^l = \frac{c_s^l}{\tilde{c}_{s,o}^l} \qquad \tilde{c}_b^l = \frac{c_b^l}{\tilde{c}_{b,o}^l} \qquad \tilde{c}_{ca}^l = \frac{c_{ca}^l}{\tilde{c}_{ca,o}^l}$$

The reduced porosities $\tilde{\phi}$, η and γ are defined as :

$$\tilde{\phi} = \frac{\phi - \phi_\infty}{1 - \phi_\infty} \qquad \eta = \frac{\phi_0 - \phi_\infty}{1 - \phi_\infty} \qquad \gamma = \frac{1 - \phi_\infty}{\phi_\infty}$$

The normalized porosity at the seafloor is given by the following relationship and porosity is maintained constant along the entire depth of the domain.

$$\tilde{\phi} = \eta = \frac{\phi_0 - \phi_\infty}{1 - \phi_\infty} = \frac{0.7 - 0.1}{1 - 0.1} = \frac{6}{9}$$

The dimensionless group Peclet number Pe_1 is characterized by the ratio of sedimentation-compaction driven fluid flux to methane diffusion.

$$Pe_1 = \frac{U_{f,sed} L_t}{D_m}$$

Similarly, Pe_2 is charaterized by the ratio of external fluid flux from deeper sediments relative to methane diffusion.

$$Pe_2 = \frac{U_{f,ext} L_t}{D_m}$$

The dimensionless group Damkohler number is characterized by the ratio of reaction to diffusion. The three Damkohler numbers for the three main reactions mentioned above are defined as follows

$$Da = \frac{\lambda L_t^2}{D_m}$$ Methanogenesis Reaction

$$Da_{AOM} = \frac{\rho_w c^w_{m,eqb}}{M_{CH_4}} \frac{\lambda_{AOM} L_t^2}{D_m}$$ Anaerobic Oxidation of Methane Reaction

$$Da_{POC} = \frac{\rho_w c^w_{m,eqb}}{M_{POC}} \frac{\lambda_{POC} L_t^2}{D_s}$$ POC dominated sulfate reduction Reaction

The mass balance equations are now complete but to obtain finite solutions, we need to specify the initial and boundary conditions.

Initial Conditions

We assume that there is zero methane, sulfate, bicarbonate, calcium and carbon isotope concentration at initial time $\tilde{t} = 0$ for any depth $\tilde{z}$.

$$\tilde{c}^l_m(\tilde{z},0) = 0 \qquad \tilde{c}^l_s(\tilde{z},0) = 0 \qquad \tilde{c}^l_b(\tilde{z},0) = 0 \qquad \tilde{c}^l_{ca}(\tilde{z},0) = 0$$

$$\delta^{13}C_{CH_4}(\tilde{z},0) = 0 \qquad \delta^{13}C_{HCO_3}(\tilde{z},0) = 0$$

Boundary Conditions

The organic solids concentration is normalized with the seafloor value, thereby specifying the normalized organic solids concentration at the seafloor to unity. Methane is assumed to form biogenically from the organic solids also refered to as Particulate Organic Carbon (POC). Sulfate, bicarbonate and calcium are normalized with its seawater values and the normalized sulfate, bicarbonate and calcium concentrations are unity at the seafloor. Carbon isotope concentrations are also normalized with respect to the seafloor value and normalized carbon isotope concentration at the seafloor is zero. External methane flux is assumed to originate in deeper sediments due to generated methane from the methanogenesis reaction. In order to incorporate the external methane flux, we specify an external methane concentration at the base of the simulation domain. Similarly, we specify a deep flux bicarbonate and calcium in our model and thus specify an bicarbonate and calcium concentration at the base of the domain whereas sulfate does not have any external flux in the system. We therefore specify a zero sulfate concentration and known methane $\tilde{c}^l_{m,ext}$, bicarbonate $\tilde{c}^l_{b,ext}$, calcium $\tilde{c}^l_{ca,ext}$and carbon isotope $\delta^{13}C_{CH_4}$and $\delta^{13}C_{HCO_3}$concentrations at the base of the simulation domain. During the methanogenesis reaction, equal amounts of methane and bicarbonate are

formed, so we equate their fluxes at the bottom boundary and we are able to specify the bicarbonate concentration equal to the methane concentration at the bottom of our simulation domain. For a corresponding bicarbonate concentration, we are able to compute a calcium concentration from the solubility product at the bottom of our simulation domain. We essentially assume dirichlet boundary conditions at the seafloor and at the bottom of the domain. Methane concentration is constrained to be zero at the seafloor and we specify a known concentration at the bottom of the domain to include the external flux coming from deeper sediments.

$$\tilde{c}_m^l(0,\tilde{t}) = 0$$
$$\tilde{c}_m^l(\tilde{L}_z,\tilde{t}) = \tilde{c}_{m,ext}^l = 1$$

where $\tilde{c}_{m,ext}^l$is the specified concentration of methane at the bottom of the domain L_z. $\tilde{c}_{m,ext}^l$is also normalized with the triple point methane solubility $\tilde{c}_{m,eqb}^l$and $L_z$is normalized with the depth of the base of hydrate stability zone and in our simulations, $\tilde{L}_z = 1$. The second boundary condition can be rewritten as follows.

$$\tilde{c}_m^l(1,\tilde{t}) = \tilde{c}_{m,ext}^l = 1$$

Sulfate, bicarbonate, calcium and carbon isotope concentrations are constrained to be seawater value at the seafloor and we specify the concentration at the bottom of the domain.

$$\tilde{c}_s^l(0,\tilde{t}) = \tilde{c}_b^l(0,\tilde{t}) = \tilde{c}_{ca}^l(0,\tilde{t}) = 1 \qquad \delta^{13}C_{CH_4}(0,\tilde{t}) = \delta^{13}C_{HCO_3}(0,\tilde{t}) = 0$$
$$\tilde{c}_s^l(1,\tilde{t}) = \tilde{c}_{s,ext}^l = 0 \qquad \tilde{c}_b^l(1,\tilde{t}) = \tilde{c}_{b,ext}^l \qquad \tilde{c}_{ca}^l(1,\tilde{t}) = \tilde{c}_{ca,ext}^l$$
$$\delta^{13}C_{CH_4}(1,\tilde{t}) = \delta^{13}C_{CH_4,ext} = -60‰ \qquad \delta^{13}C_{HCO_3}(1,\tilde{t}) = \delta^{13}C_{HCO_3,ext} = +10‰$$

where $\tilde{c}_{s,ext}^l$, $\tilde{c}_{b,ext}^l$, $\tilde{c}_{ca,ext}^l$, $\delta^{13}C_{CH_4}$and $\delta^{13}C_{HCO_3}$are specified external concentrations of sulfate, bicarbonate, calcium and carbon isotope in methane and bicarbonate at the bottom of the domain $L_z$normalized with the seawater concentrations $\tilde{c}_{s,c}^l$, $\tilde{c}_{b,c}^l$ and $\tilde{c}_{ca,c}^l$.

Numerical Solution for Coupled Mass balances with reactions

To simplify the problem, we started simulating individual methane and sulfate profiles considering them to be present as single components and modeled a simple convection diffusion problem. We computed the individual profiles and were also able to compute the fluxes and our results were analogous to a conventional convection diffusion solution. To take a leap forward, we coupled the methane and sulfate mass balances and include all the important

reactions in our model. For the moment, we just include the AOM reaction and the calcite precipitation reaction in the coupled methane, sulfate, bicarbonate and calcium mass balance equations and compute the four profiles simultaneously considering all of them to be present in the system. We have included methanogenesis and the POC driven reaction as well, but set a parameter to zero for the time being to make that source/sink term negligible in our model. We specify values for all our parameters and dimensionless groups as shown below.

$$\mathrm{Da} = 5 \qquad \mathrm{Da}_{AOM} = 10^{8} \qquad \mathrm{Da}_{POC} = 10^{-4}$$

$$\tilde{\mathrm{D}}_{S} = \frac{\mathrm{D}_{S}}{\mathrm{D}_{m}} = \frac{0.56\times10^{-9}}{0.87\times10^{-9}} = 0.64 \qquad \tilde{\mathrm{D}}_{b} = \frac{\mathrm{D}_{b}}{\mathrm{D}_{m}} = \frac{0.87\times10^{-9}}{0.87\times10^{-9}} = 1$$

$$\tilde{\mathrm{D}}_{Ca} = \frac{\mathrm{D}_{Ca}}{\mathrm{D}_{m}} = \frac{0.4\times10^{-9}}{0.87\times10^{-9}} = 0.46$$

$$\alpha_{0} = 1 \qquad \beta = 0 \qquad Pe_{1} = 0$$

$$Pe_{2} = [-0, -1, -2, -5, -6, -8, -10, -12, -15, -20]$$

The methane and sulfate profiles are computed and shown below in figure 6.8.3. The profiles show that methane concentration is constrained at the specified value at the bottom of the simulation domain and methane coming from below is transported towards the seafloor due to advective fluid flux. The advective fluid flux increases with increase in Pe_2 and the profiles go straight up towards the seafloor before it gets constrained at the SMT to zero methane concentration due to the AOM reaction. Near the SMT the diffusion gradients build up and methane profiles tend to bend towards the zero concentration at the SMT. For zero Pe_2, thereby assigning, zero total fluid flux, profiles are linear and represent pure diffusion system.

The sulfate concentrations have the seawater value at the seafloor and when the concentrations are normalized with the seawater value, they attain a unit value at the seafloor $\tilde{z} = 0$. The normalized concentrations are constrained to zero at the SMT when sulfate is consumed by methane via the AOM reaction.

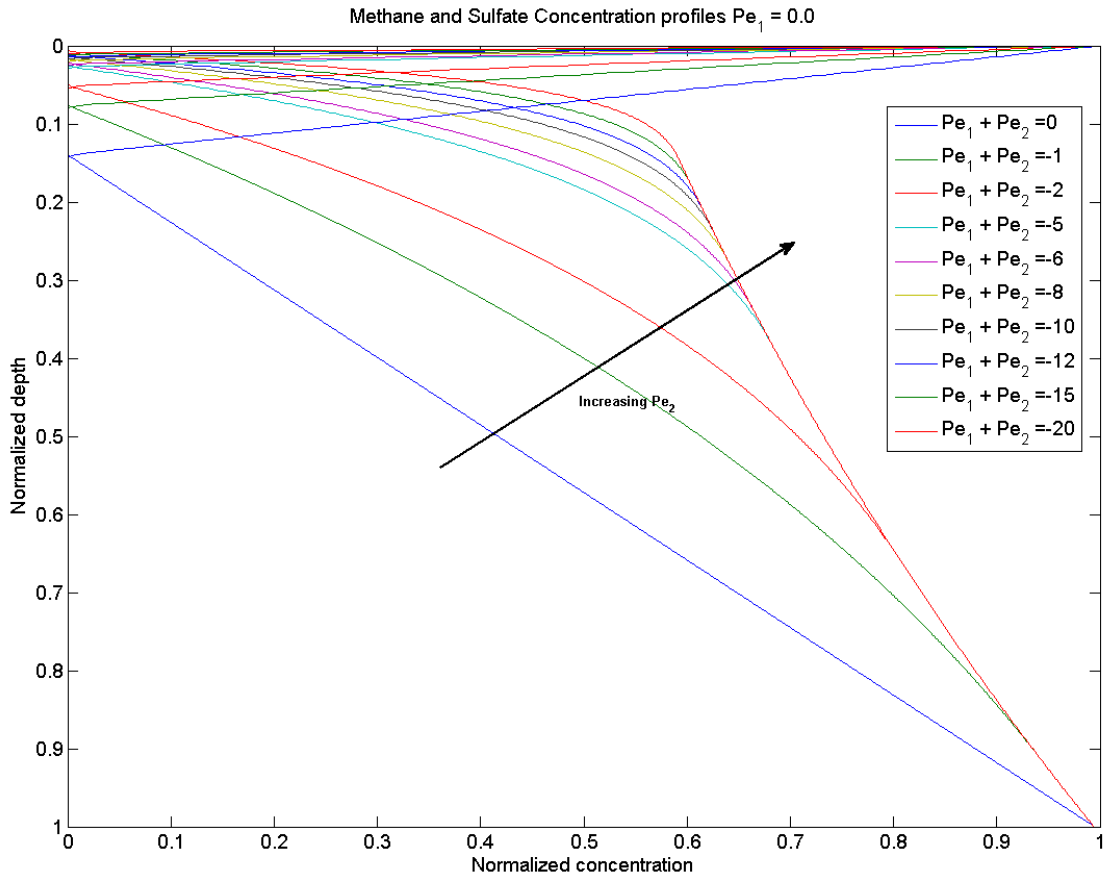

Figure 6.8.3: Normalized methane and sulfate concentration profiles for Pe_1=0 at dimensionless time $\tilde{t} = 2.0$. The arrow shows the direction of increasing Pe_2.

We plot the Bhatnagar's results for Pe_1 + Pe_2 on the same plot with our numerical solution as shown in figure 6.8.4. The plot is then zoomed in to observe the concentration gradients near the seafloor. Our solution lies right on top of Bhatnagar's solution which verifies our numerical solution and makes it reproducible.

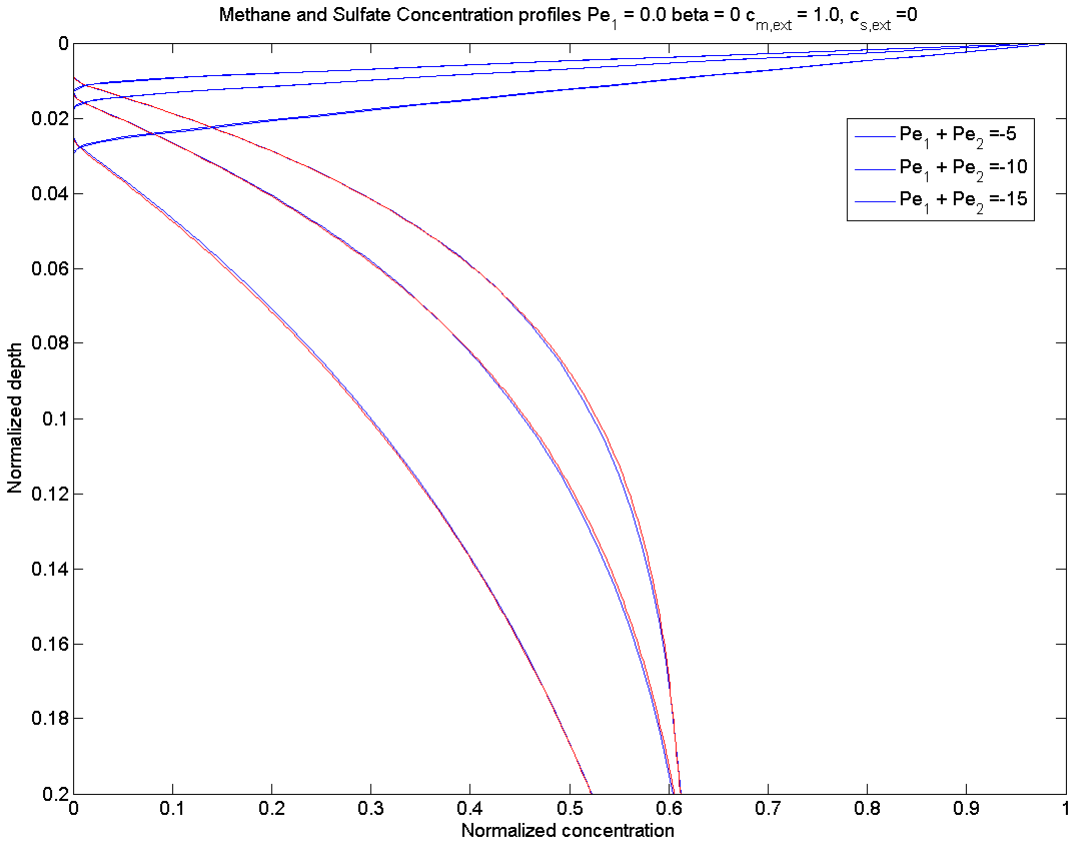

Figure 6.8.4: Normalized methane and sulfate concentration profiles for Pe_1=0 at dimensionless time $\tilde{t} = 2.0$

From the above plots, we realize one very important observation that the depth of SMT reduces and becomes shallower with increase in Pe_1 + Pe_2 (net flux). As Pe_1 + Pe_2 increases, the SMT depth is shifted to a shallower depth and we plot the SMT depth with the Pe_1 + Pe_2 in figure 6.8.5.

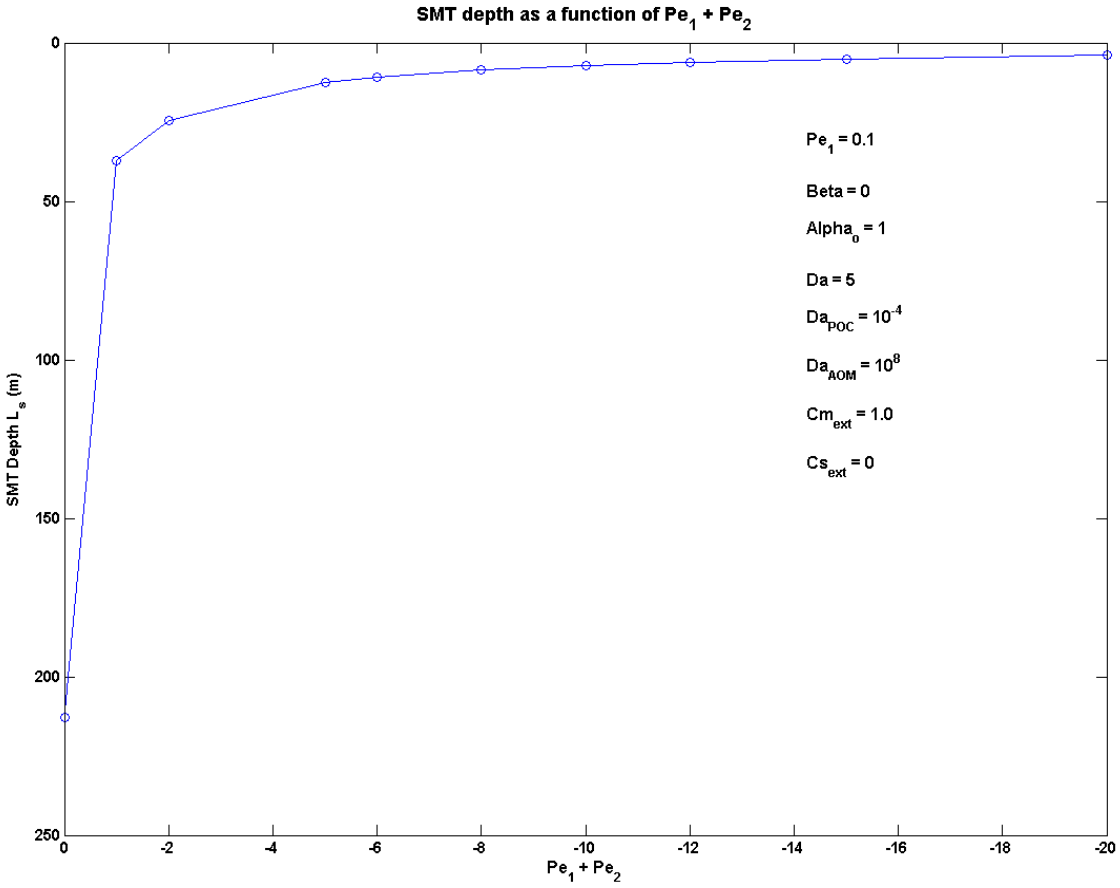

Figure 6.8.5: SMT depth as a function of Pe_1+ Pe_2 shows that with increase in Pe_1 + Pe_2, the SMT depth becomes shallower. SMT depth is expressed in meters below the seafloor (mbsf).

In the above plot, SMT depth and Pe_1 + Pe_2 were normalized with L_i which overspecified the problem to an extent. To remove this overspecification, we renormalize the two parameters with L_s. With this renormalization, we plot the product of SMT depth and Pe_1 + Pe_2 as a function of Pe_1+ Pe_2 as shown in figure 6.8.6.

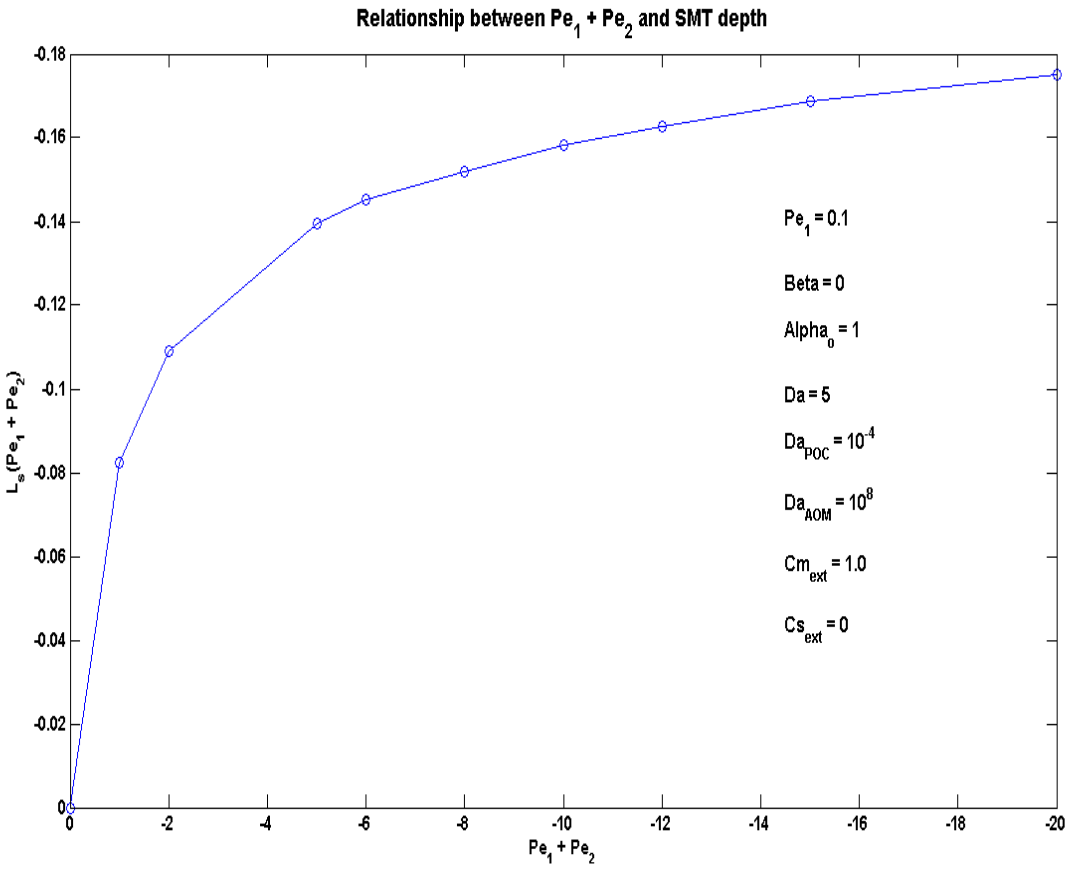

Figure 6.8.6: Product of SMT depth and $Pe_1 + Pe_2$ as a function of $Pe_1 + Pe_2$ ensured both the variables were normalized with L_s

The model is not complete with just the sulfate and the methane profiles. Bicarbonate and calcium profiles give us a better understanding of the contribution of the deep bicarbonate flux. As explained previously, the bicarbonate is generated in the system because of AOM reaction, POC driven sulfate consumption reaction and the methanogenesis reaction. In our current model, we assume, bicarbonate generation from AOM reaction only and bicarbonate consumption by calcite precipitation reaction since POC reaction is neglected currently in the model. The bicarbonate profiles are constrained at the external concentration of bicarbonate $\tilde{C}^{l}_{b,ext}$ at the base of the domain. Bicarbonate profiles are expected to increase till the SMT depth because of AOM reaction and then concentration drops because of calcite precipitation and the profiles finally get constrained at the specified bicarbonate concentration near the bottom of the domain. However, we are making some more changes to the bicarbonate mass balance equations as a result of the sink due to calcium carbonate precipitation which has been included in our model recently, so the bicarbonate profiles have not been included in this report.

The calcium profiles are also constrained to unity at the seafloor and calcium present in the system is precipitated as calcite when it reacts with the bicarbonate formed in the system. This reduces the calcium concentration to finite equilibrium value which can be obtained from the solubility product of calcium carbonate $K_{SP_{CaCO_3}} = 8.5 \times 10^{-9}$ when the species concentrations are expressed in moles/litre. The calcium in the system is the limiting reagent and gets consumed when it reacts with bicarbonate until the concentration reaches the equilibrium concentration beyond which calcium concentration cannot reduce any further.

$$K_{SP_{CaCO_3}} = \left[Ca^{2+}\right]\left[CO_3^{2-}\right] = 9.237e^{-0.0277T} \times 10^{-9} = 8.5 \times 10^{-9} \qquad \text{at} 3^{o}C$$

From the mass balance equations, we can compute the calcium concentration profiles which is consumed by the bicarbonate in the calcite precipitation reaction and forms calcium carbonate. As long as the product of the calcium and bicarbonate concentration is greater than the solubility constant, we are able to compute the concentration of calcium carbonate from the solubility product mentioned above. As soon as calcium concentration reduces to equilibrium concentration, it cannot reduce any further and calcium carbonate stops precipitating. This calcium carbonate formation is the sink for the bicarbonate and calcium and has been included in our model recently. We are still trying to compute the calcium profiles with the carbonate precipitation correction so it has not been included in this report.

The carbon isotope $\delta^{13}C$ concentration profiles in bicarbonate (DIC) are also computed. The normalized carbon isotope in DIC is zero at the seafloor and it reduces to a negative value of around -25‰ which is due to combination of -60‰ from bicarbonate formed at SMT because of AOM reaction and due to the +10‰ from deep flux bicarbonate coming from below. It starts increasing and finally gets constrained to 10‰ at the bottom of the domain where we have maintained constant boundary condition at the lower boundary due to the external flux of bicarbonate in deeper sediments.

So far, we have only included AOM, effectively neglecting the POC reaction completely. Most of the data can be explained in this way, much as anticipated by our straightforward arguments (Dickens and Snyder, 2009). We should, however, include the POC reaction and consider zero fluxes to fully evaluate the alternative interpretation (Kastner et al., 2008). In due course, we plan to include both reactions with the two interpretations of data as two end members. Revisiting Gaurav's 1-D model as a part of task 6.8(b) has helped us to reconcile the contradiction between the two groups and also helped us understand how sulfate, bicarbonate, calcium and carbon isotope profiles can be used as a tool to interpret methane flux.

Abstract selected for Oral Presentation scheduled on December 17, 2009 at the AGU Fall meeting 2009 in San Francisco, CA

Sulfate, Methane, Alkalinity, Calcium and Carbon Isotope ($\delta^{13}C$) Profiles as an Indicator of Upward Methane Flux

Sayantan Chatterjee[1], Gaurav Bhatnagar[2], Walter G. Chapman[1], Gerald R. Dickens[3], Brandon Dugan[3], George J. Hirasaki[1]

The upward flux of methane is an important determinant for the amount of hydrate that may potentially be present in the sediments. One approach to measure methane flux is to relate sulfate methane transition (SMT) depth to the methane flux via anaerobic oxidation of methane (AOM) (Borowski *et al.*, 1996; Dickens and Snyder, 2009). However, numerous prominent authors such as Kastner argue that consumption of pore water sulfate in shallow sediments is a result of oxidation of particulate organic carbon (POC) as opposed to methane. Another contradictory argument between these two groups is based on the carbon isotopic composition ($\delta^{13}C$) of dissolved inorganic carbon (DIC) across the SMT. The articles in *Fire in the ice* by Kastner *et al*. (2008) and Dickens and Snyder (2009) focus on these two important arguments in the gas hydrate community and warrant more detailed modeling to help resolve the questions raised by these two groups.

We examine the two hypotheses by the two groups and reconcile their interpretations using Bhatnagar's 1-D model (2008). This model computes mass balances with both advective and diffusive fluxes. In addition to the mass balances, sulfate consumption reactions following the two pathways (i.e.: POC driven and anaerobic oxidation of methane) have been included in the current model. Setting the model parameters to represent zero net flux, and thus assuming a closed system, we are able to justify Kastner's interpretations. Bicarbonate (DIC) or alkalinity, Ca^{2+} (for calculating carbonate precipitation), and $\delta^{13}C$ in DIC profiles are computed in addition to the sulfate and methane profiles along depth to provide an understanding of the contribution due to the deep bicarbonate flux. This deep flux of bicarbonate profile would validate Dickens' interpretations and justify the dominance of the AOM reaction for consumption of sulfate in shallow sediments. This model serves as a tool to interpret methane flux with the help of pore water sulfate profile along with bicarbonate (alkalinity) and $\delta^{13}C$ in DIC balances to reconcile both hypotheses claimed by the two groups.

[1]Rice University, Department of Chemical and Biomolecular Engineering, Houston, Texas 77251
[2]Shell Global Solutions (US) Inc, Houston, Texas 77210
[3]Rice University, Department of Earth Science, Houston, Texas 77251

References

Bhatnagar, G., Chapman, W. G., Dickens, G. R., Dugan, B., and Hirasaki, G. J. (2008), Sulfate-methane transition as a proxy for average methane hydrate saturation in marine sediments. *Geophys. Res. Lett.*, 35, L03611,doi:10.1029/2007GL032500.

Bhatnagar, G., Chapman, W.G., Dickens, G.R., Dugan, B. and Hirasaki, G.J. (2007), *Generalization of gas hydrate distribution and saturation in marine sediments by scaling of thermodynamic and transport processes*, *Am. J. Sci*., 307: p 861-900

Borowski, W. S., Paull, C. K., and Ussler III, W. (1999) Global and local variations of interstitial sulfate gradients in deep-water, continental margin sediments: Sensitivity to underlying methane and gas hydrates. *Mar. Geol.*, 159:131–154

Dickens, G.R., Snyder, G. (2009), Interpreting upward methane flux, Fire in the Ice, Winter, p 7-10

Kastner, M., Torres, M., Solomon, E., and Spivack, A. J. (2008), Marine pore fluid profiles of dissolved sulfate: do they reflect in situ methane fluxes? Fire in the ice, Summer, p 6-8

Task 7: Analysis of Production Strategy

J. Phirani & K. K. Mohanty, University of Texas at Austin

Abstract

Experimental data on multiphase flow properties of gas hydrate containing sediments is rarely available. Empirical correlations are often used for transport properties of sediments containing gas hydrates. In this work, we have developed mechanistic models for transport properties for hydrate bearing sediments. Hydrate deposition and dissociation is modeled in a single pore to develop pore-scale laws of hydrate occupancy. Pore size distributions are found for sediments containing different particle size distributions. Pore size distribution is modified due to hydrate deposition. Percolation theory is used to numerically calculate effective transport properties at different hydrate and water saturations. The transport properties calculated from these mechanistic models can replace the empirical correlations in reservoir simulations of hydrate reservoirs.

Methodology

Porous Medium Generation

Shallow marine sediments are unconsolidated structures of sand, silt, and clays. We consider spherical particles with a Gaussian radius distribution. To generate the porous medium, particles are initially placed randomly in space confined by a rectangular cuboid of specific length, width and height. The dimensions of the cuboid are chosen such that about 30,000 particles can be conveniently placed inside. The particles are initially non-overlapping with zero initial velocity and are allowed to settle under gravity using discrete element method (DEM) (Cundall and Strack, 1979). The simulation is performed until all the particles have equilibrated with each other and their velocities are close to zero. The simulation gives the final position of the particles along with their respective radii. The pore throat and pore body size distributions and coordination numbers are calculated by Delaunay triangulation (Cignoni et al., 1998).

Transport Property Calculation

Percolation theory was used to calculate the transport properties (permeability, and relative permeabilities of wetting and non-wetting fluids) of the medium (Heiba et al. 1992, Heiba et al. 1984). We assume a Bethe network of pore throats. All the resistance to flow and the volume of the pore structure are assumed to be in pore throats. A coordination number of 5 is assumed for the present case. The flow rate through a single pore segment is given by:

$$q=g(\Delta P/\mu) \quad (1)$$

where q is the flow rate, g is the conductance, ΔP is the pressure drop and μ is the viscosity of the fluid flowing. The conductance distribution of the network is given by:

$$G(g)=(1-Q)\delta(g)+QG'(g) \quad (2)$$

where Q is the fraction of pores allowed and $G'(g)$ the probability that conductance of an allowed pore lies between g and $g+dg$. For phase j the conductance distribution is given by:

$$G(g)=(1-Q_j)\delta(g)+Q_jG_j'(g) \quad (3)$$

where Q_j is the fraction of pores allowed and $G_j'(g)$ the probability that conductance of an allowed pore lies between g and $g+dg$.

The relative permeability k_{rj} of phase j is calculated as:

$$k_{rj} = g_j/g0 \quad (4)$$

where g_j is conductance of phase j and g0 absolute conductance of the network. Conductance for Bethe network for phase j is defined as:

$$g_j=-nC'(0) \quad (5)$$

where *n* is coordination number of the Bethe network used. Function C(x) is solution of the following equation in Laplace form:

$$\int_0^\infty e^{-tx} C(x)dx = \frac{1-Q_j}{t} + Q_j \int_0^\infty \alpha_j^A \left|\frac{dr}{dg}\right| dg \left\{ \frac{1}{t+g} + \frac{g^2}{(t+g)^2} \int_0^\infty \exp\left(\frac{-gt}{g+t} x\right) [c(x)]^{n-1} dx \right\} \quad (6)$$

where, Q_j is allowed fraction of pores for phase *j*, *g* is the conductivity of the pore structure, and $\alpha_j^{\prime}$ is the radius distribution of allowed pores for phase *j*. Absolute permeability is obtained when allowed fraction of pore is 1 and allowed radius distribution is the same as radius distribution of the network. The algebraic solution of the above equation to find *C'(0)* is given by Heiba et al. (1984). The relative permeabilities and the absolute permeability are calculated for the pore network.

Effect of Hydrate Saturation on Pore Structure: Hydrate deposition from flow of methane-saturated water was simulated in several cylindrical pores. This simulation showed that the hydrate saturation in a particular pore is independent of the size of the pore. The thickness of hydrate deposited on the wall is given by:

$$t_s = r\left(1 + \sqrt{1 - SH}\right) \quad (7)$$

where, t_s is thickness of hydrate layer, *r* is the original radius of the pore and *SH* is hydrate saturation. New radius distributions are calculated for different hydrate saturations. Percolation theory is used with the new radius distribution to calculate the transport properties for a given hydrates saturation. A correlation dependent on hydrate saturation, wetting fluid (water) saturation and non wetting fluid (gas) saturation is developed for a particular radius distribution.

Results

Spherical particles of Gaussian radius distributions were packed using the DEM method. The pore throat radius distribution was determined after Delaunay triangulation. The pore throat distribution of the porous medium formed by the

particles having Gaussian particle radius distribution is given by Rayleigh distribution. Table 1 shows the different distributions studied.

Particle size distribution		Radius distribution
Mean (μm)	Variance (μm)	σ (μm)
200	50	33.71
200	75	58.46
200	100	157.4
100	50	88.1
50	50	13.86

Figure 1 shows the water and gas relative permeabilities from percolation theory for the base case porous medium with zero hydrate saturation when σ for Rayleigh distribution is 157.

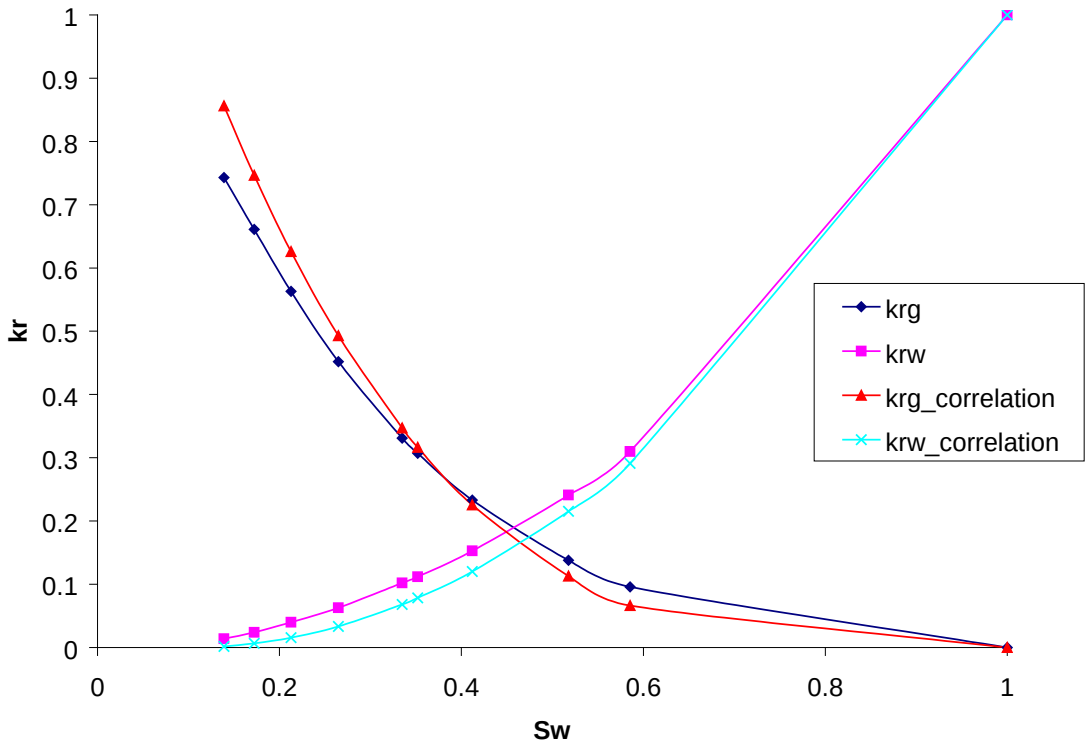

Figure 1: Relative permeability of the sediment without hydrate

The following correlation is developed for relative permeability by matching the results of the percolation theory:

$$k_{rw} = \left(\frac{S_w - S_{wr}}{1 - S_{wr}} \right)^2 \qquad (8a)$$

$$k_{rg} = \left(\frac{1 - S_w}{1 - S_{wr}} \right)^{3.5} \qquad (8b)$$

where k_{rw} is relative permeability of water or the wetting phase and k_{rg} is relative permeability of gas or the nonwetting phase.

Figure 2 shows the relative permeability obtained from percolation theory for the base case at different hydrate saturations. The curvature of relative permeability curves increase with increasing hydrate saturation.

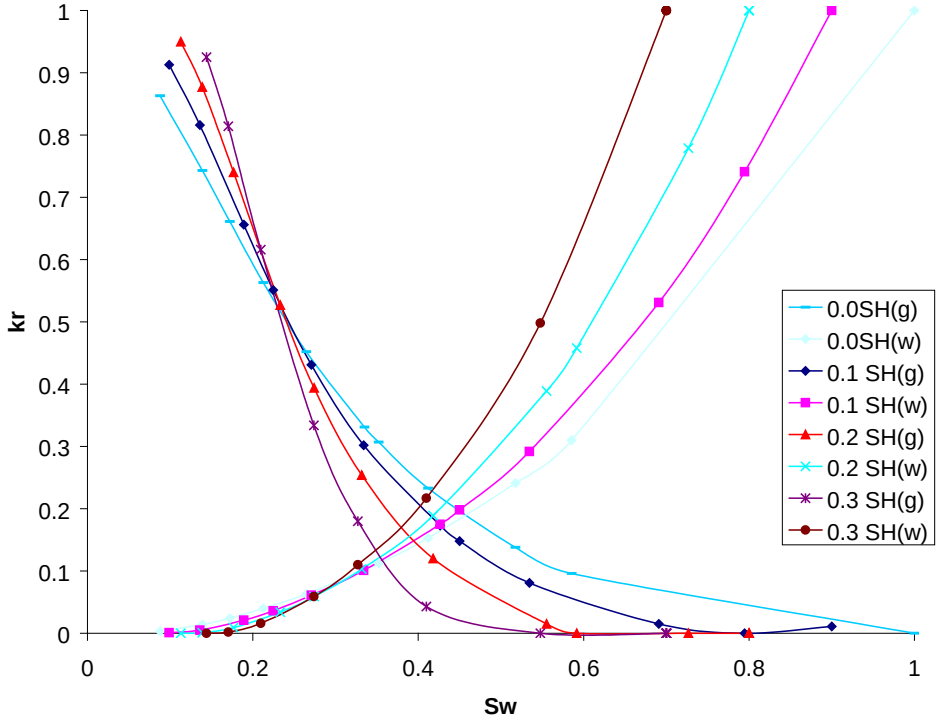

Figure 2(a): Relative permeability curves for different hydrate saturations

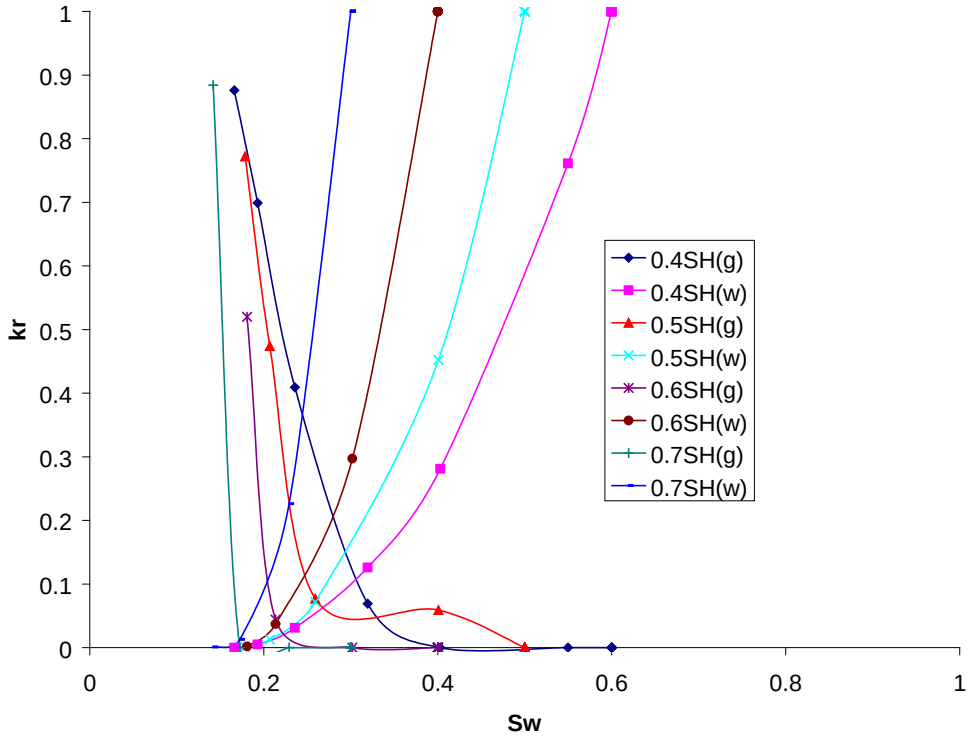

Figure 2(b): Relative permeability curves for different hydrate saturations

A correlation was developed between the computed relative permeability and hydrate saturation. The following correlation finds the best fit with the percolation theory results.

$$k_{rw} = \left(\frac{S_w - S_{wr}}{1 - S_H - S_{wr}} \right)^{(2+2S_H)} \tag{9a}$$

$$k_{rg} = \left(\frac{1 - S_H - \beta S_w^{\alpha}}{1 - S_H - S_{wr}} \right)^{(3.5-S_H)} \tag{9b}$$

$\alpha = 2,\ S_H \geq 0.5$

$= 1,\ S_H \leq 0.2$ (9c)

$= 3.25S_H + 0.425,\ 0.2 < S_H < 0.5$

$\beta = 10S_H - 1,\ S_H > 0.1$

$= 1,\ S_H \leq 0.1$ (9d)

Figure 3 shows comparison of relative permeability curves for 2 hydrate saturations (0.4 and 0.6) obtained from percolation theory and the correlations developed in Eq. (9).

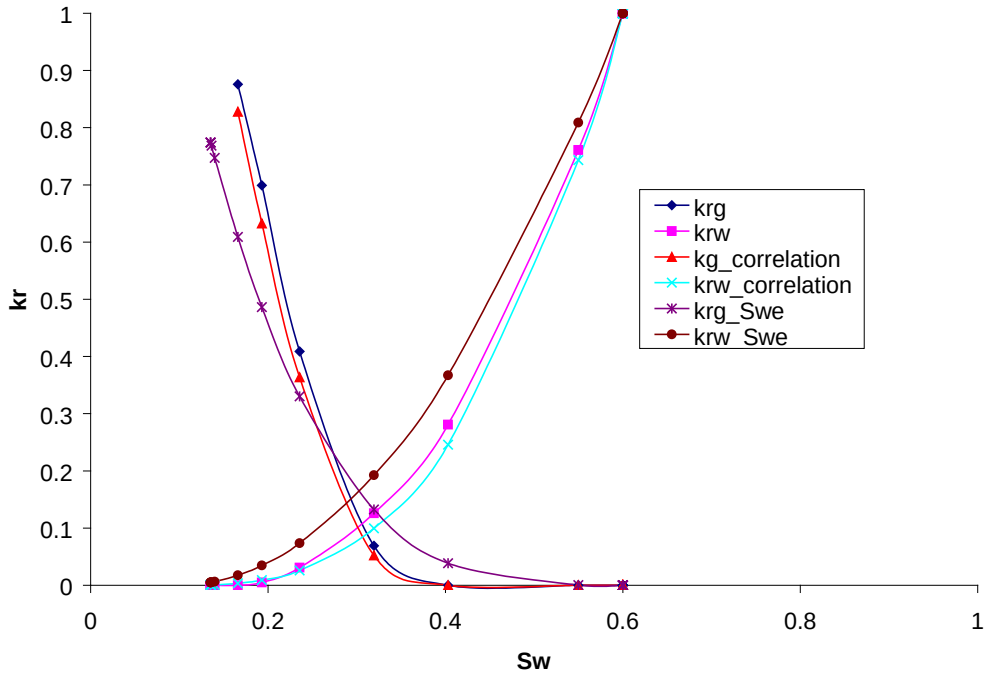

Figure 3(a): Relative permeability of the sediment for hydrate saturation 0.4

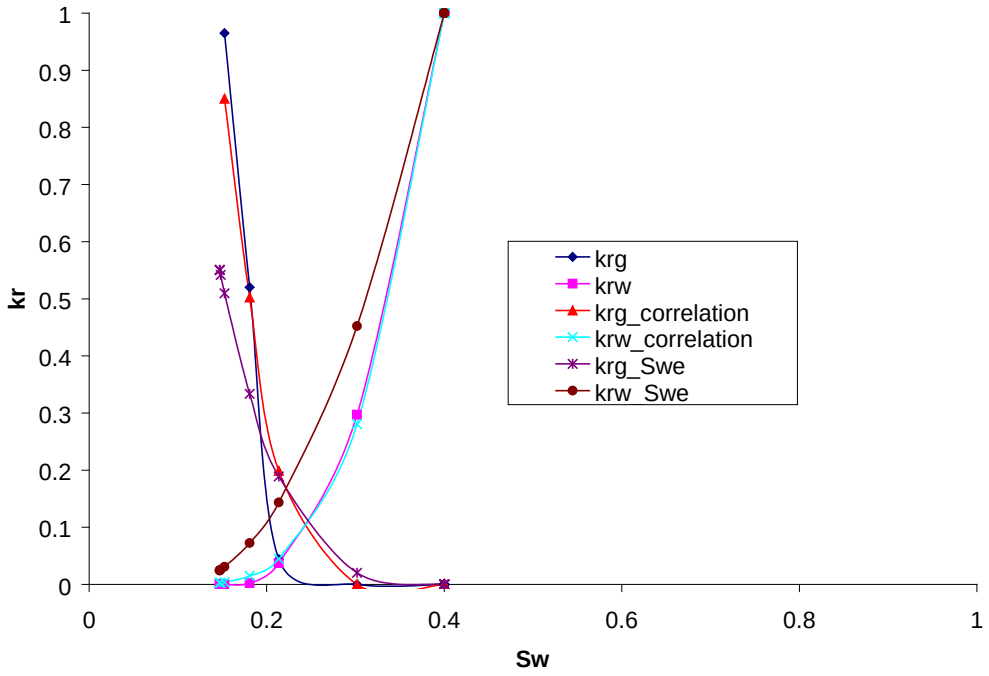

Figure 3(b): Relative permeability of the sediment for hydrate saturation 0.6

This shows that the correlation in equation 14 is valid for normal distribution of particle size which gives Rayliegh pore radius distribution.

Conclusions

- When hydrates deposit from a solubilized brine phase, hydrates deposit on walls of pore and pore-scale hydrate saturation is independent of size.
- Normal distribution of particle size of spherical sediments gives Rayleigh distribution of pore throat radius.
- For Rayleigh throat radius distribution, relative permeability matches Corey correlation with ng = 3.5 and nw = 2.
- With increasing hydrate saturation, the gas exponent ng decreases and water exponent nw increases.
- Using effective fluid saturations to calculate relative permeability in the presence of hydrates does not agree with calculated relative permeabilities.

Future Work

Relative permeability curves depend on the shape of throat radius distributions. Transport properties would be developed for other particle size and pore size distributions. These transport properties would be used in reservoir simulations of hydrate bearing sediments.

Presentations & Publications

1. Phirani, J., Mohanty, K. K. & G. Hirasaki, “Warm Water Flooding of Unconfined Gas Hydrate Reservoirs,” *Energy & Fuels* (2009), doi:10.1021/ef900291j.

2. Phirani, J. & Mohanty, K. K., “Warm Water Flooding of Confined Gas Hydrate Reservoirs,” *Chem. Eng. Sci.*, 64, 2361-2369 (2009). doi:10.1016/j.ces.2009.02.019.

3. Phirani, J., Pitchumani, R., & Mohanty, K. K., “Transport Properties of Hydrate Bearing Formations from Pore-Scale Modeling,” SPE 124882, Proceedings of SPE ATCE, New Orleans, LA, Oct. 4-7, 2009.

Task 8: Seafloor and Borehole Stability: Hugh Diagle and Brandon Dugan

Summary
We primarily focused on modeling of sediment instability associated with hydrate accumulations (Subtask 8.2) that builds on our work of sediment-hydrate properties (Subtask 8.1) because the models use these properties as inputs. We are continually extending our collaborations and data integration (Subtask 8.3) as we test the instability models against field data collected by DOE, IODP, and other international programs.

Milestone Status
8.1c Complete database – manuscript has been submitted, revised, and resubmitted to Reviews of Geophysics.

8.2a Link database with models – models for slope stability and fracture genesis are using properties based on the database.

8.2b Add sediment stability to models – initial stability models for slope failure and fracture genesis have been implemented and are being tested. We are now testing against field data and will soon begin sensitivity analysis and summary.

8.2c Conditions for (in)stability – this is ongoing work and will be completed but delayed until 06/10 as we are progressing in phases. We developed new models on fracture genesis that were not in the original proposal, but that were deemed important when looking at hydrate distribution in fine-grained systems. These fracture models are the focus of one manuscript that will be submitted in 2009. Full-scale stability and slope failure models will incorporate our fracture work but will not be completed until 2010.

Subtask 8.1: Sediment-Hydrate Properties
This task has been completed with a manuscript that has been submitted to Reviews of Geophysics. We are awaiting final acceptance and publication of the manuscript.

Subtask 8.2: Modeling (In)stability
Our instability work has been the most productive task in 2009 as we have developed new fracture genesis and fracture fill models. This work has been pushed to the forefront as the sediment-hydrate properties research showed a dearth of data in fine-grained systems and numerous marine field programs have shown the importance of fractures controlling hydrate saturation and distribution in fine-grained sediments. These fractures most likely are an important control for fluid migration between high permeability units which are also known to yield concentrated hydrate accumulations. This work led to the DOE/NETL Methane Hydrate Fellowship to Hugh Daigle, a Ph.D. student in our group.

Daigle has been investigating the factors which can lead to fracture-hosted hydrate deposits such as those observed at Hydrate Ridge, Keathley Canyon Block 151, and the Krishna-Godavari Basin offshore India. The goal of this work is to determine how hydrate formation can cause fracture formation

either by pore pressure buildup or by frost heave. Ultimately this will be used to evaluate heterogeneous hydrate saturation and constrain a mechanism for gas migration and enhance hydrate accumulation in coarse-grained intervals.

The model builds on the methods of Bhatnagar et al. (2007) to compute the kinetics of hydrate formation. Hydraulic fractures may occur when the pore pressure in the system exceeds the minimum horizontal stress, which is taken to be 90% of the total vertical stress (Finkbeiner et al., 2001). As hydrate forms, the pores are occluded, which decreases the permeability and increases the pressure gradient required to maintain a constant flow rate. The model is run to the point where hydraulic fractures form. Daigle computes the hydrate heave force, which is the force exerted by a growing hydrate lens on the surrounding sediment (Rempel, 2007):

$$\vec{\mathbf{F}} = \frac{\rho_h \mathcal{L}}{T_m}\left(T_m - T_l - \int_{T_l}^{T_f} \phi S_h dT\right) \quad , \qquad \text{(Equation 1)}$$

where ρ_h is the bulk density of hydrate [kg m^{-3}], L is the latent heat of fusion per unit mass [J kg^{-1}], T_m is the melting temperature (three-phase equilibrium temperature) of hydrate at a given depth [K], T_l is the in situ (lens) temperature [K], T_f is the temperature at the base of the MHSZ [K], S_h is the hydrate saturation [m^3 m^{-3}], and $\vec{\mathbf{n}}$ is the outward unit normal vector. We assume ρ_h = 930 kg m^{-3} (Davie & Buffett, 2001) and L = 5.47x10^5 J kg^{-1} based on a latent heat of fusion per mole of 6.54x10^4 J mol^{-1} and a molar mass of 0.1196303 kg mol^{-1} for $CH_4 \cdot 5.75H_2O$ (Sloan, 1990).

We have run four scenarios based on field studies: Keathley Canyon Block 151 (KC151), Blake Ridge, Hydrate Ridge, and India National Gas Hydrate Program (NGHP) Site 10. These sites have been characterized in terms of porosity and permeability profiles. At KC151, a maximum vertical flow rate of 0.491 mm yr^{-1} can be sustained by the sediments; this results in fracture formation after 6.98x10^5 years (Figure 1). At Blake Ridge, Daigle uses a vertical flow rate of 0.2 mm yr^{-1} based on porewater chemistry constraints (Egeberg & Dickens, 1999). This results in fracture formation after 8.12x10^6 years (Figure 2). At Hydrate Ridge, we use a vertical flow rate of 300 mm yr^{-1} (Torres et al., 2002), which results in fracture formation after 9030 years (Figure 3). At NGHP Site 10, we use a vertical flow rate of 41 mm yr^{-1}, which results in fracture formation after 1.11x10^5 years (Figure 4). Vertical flow rates at this site are not constrained, but the value Daigle uses gives hydrate saturations which are very close to those determined from pressure cores (Lee & Collett, 2009). The hydrate saturations required to produce hydraulic fracturing increase with the amount of time required; for example, at Blake Ridge, the maximum hydrate saturation is 99.3%, while at Hydrate Ridge the computed hydrate saturation is near 50%. The hydrate heave force is sufficient to create sub-vertical veins in all situations over all but the lowest 20% of the hydrate stability zone. Based on time constraints, it appears that hydraulic fracturing by pore pressure buildup is feasible only at Hydrate Ridge and possibly NGHP Site 10; it is unlikely that Blake Ridge and KC151 could have maintained steady-state flow for ~10^6 years. However, we

conclude that hydrate heave is an effective means of generating sub-vertical fractures and veins in all situations in a short period of time.

To investigate the role of heterogeneity, Daigle modeled Hydrate Ridge as a series of alternating high- and low-permeability layers based on log data. He used log data from borehole 1250B to divide the sedimentary column into zones of similar porosity; and then assigned a constant permeability of 10^{-14} m^2 to the zones with porosity greater than 59% and a constant permeability of 10^{-15} m^2 to the zones with porosity less than 59%. In this model, hydraulic fractures form after 970 years in the middle of the hydrate stability zone near 70 mbsf at the base of a low-permeability layer (Figure 5); hydrate saturations are near 5% over the hydrate stability zone. The heterogeneous case allows fractures to form in the middle of the stability zone, and shows that fractures will form preferentially at the base of lower-permeability layers, which confirms the hypothesis of Weinberger & Brown (2006) that the hydrate distribution at Hydrate Ridge can be ascribed to preferential formation of hydrates in higher-permeability layers connected by fractures through lower-permeability layers. Additionally, the heterogeneous model requires less hydrate for fractures to form, and the resulting hydrate saturations are closer to those inferred from logs (Lee & Collett, 2006).

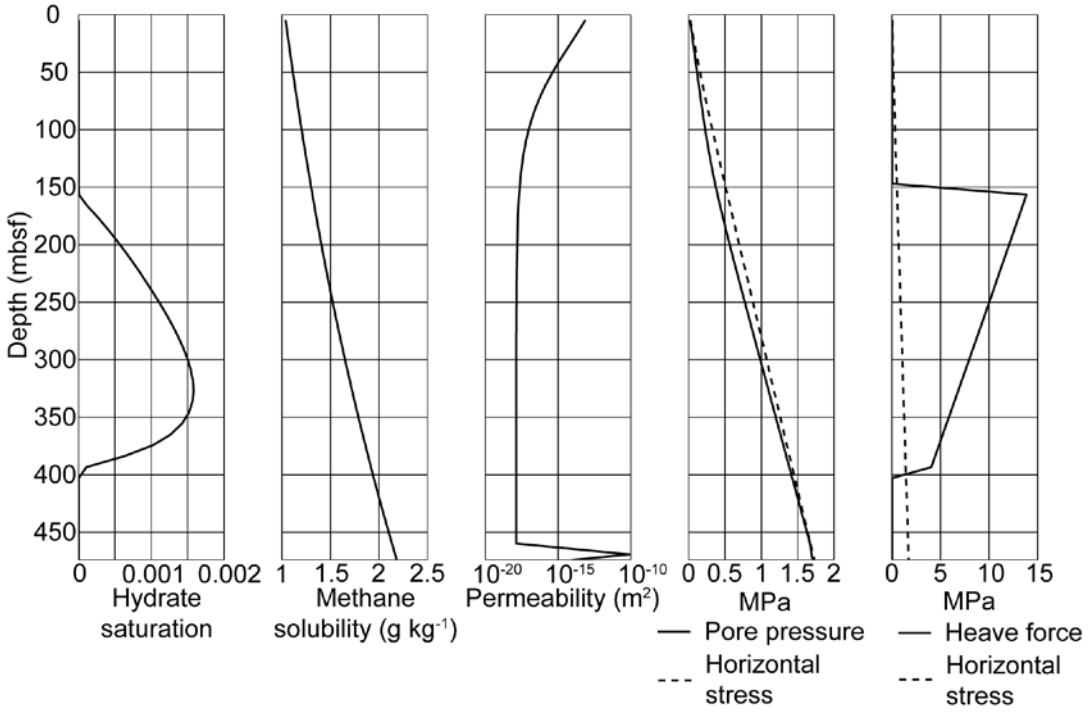

Figure 1. Model results for Keathley Canyon Block 151 using a flow rate of 0.491 mm yr^{-1}. Fracturing occurs after $6.98x10^5$ years. Hydrate heave force is computed from Equation 1.

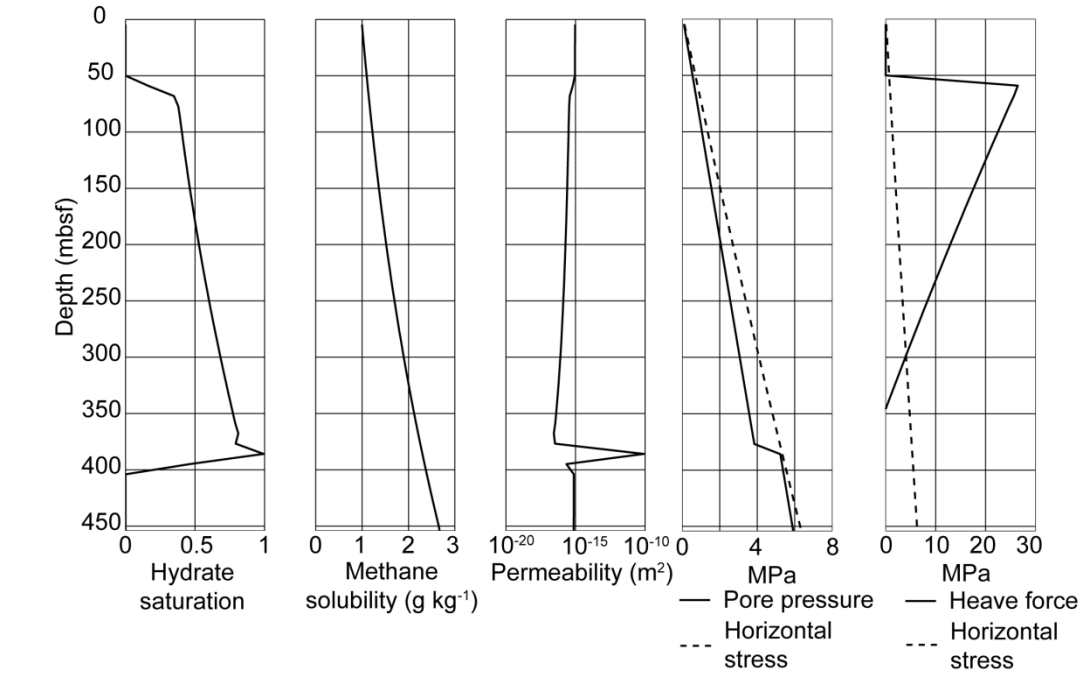

Figure 2. Model results for Blake Ridge using a flow rate of 0.2 mm yr^{-1}. Fractures occur after $8.12x10^6$ years.

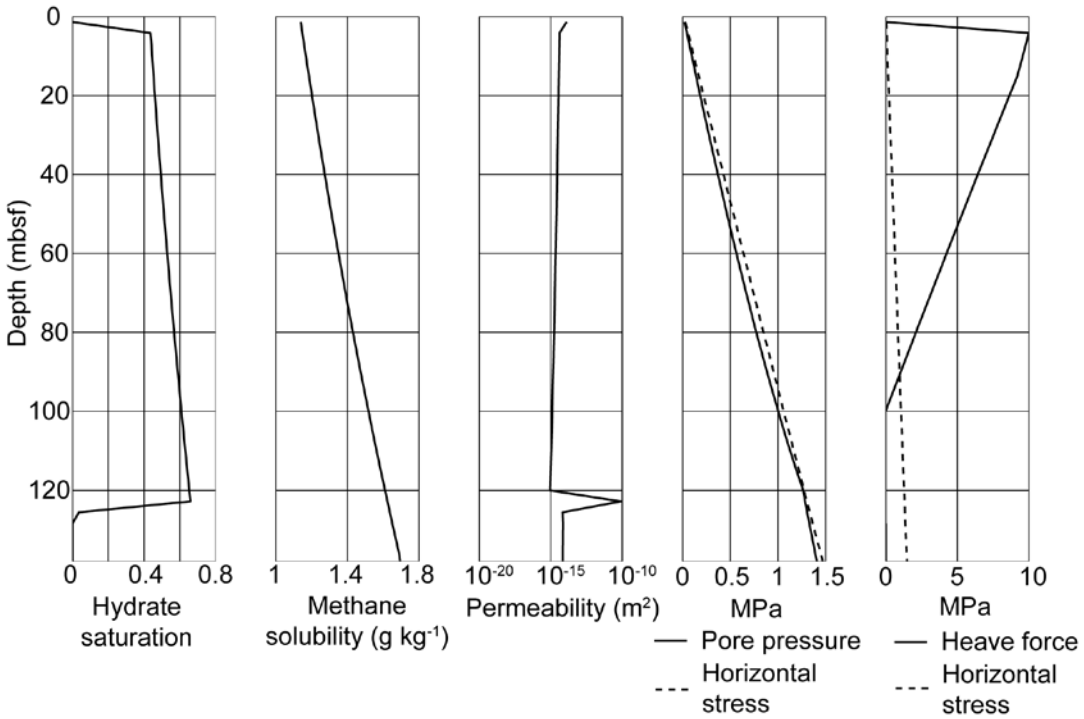

Figure 3. Model results for Hydrate Ridge using a flow rate of 300 mm yr^{-1}. Fractures occur after 9030 years.

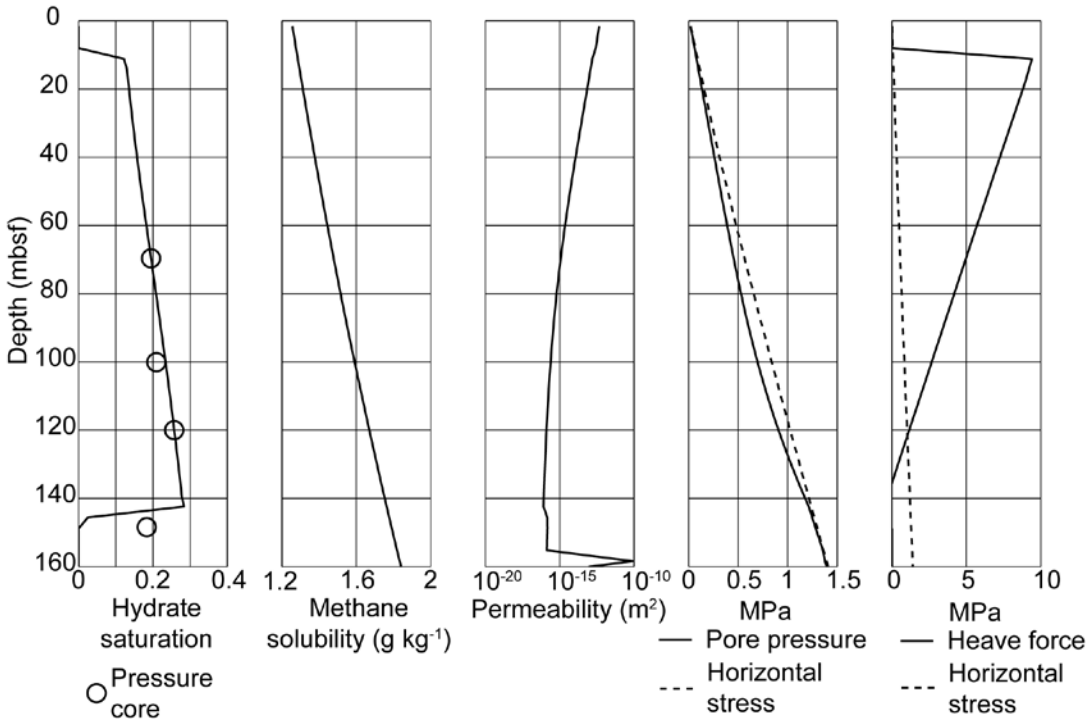

Figure 4. Model results for NGHP Site 10 using a flow rate of 41 mm yr^{-1}. Fractures occur after $1.11x10^5$ years. Hydrate saturations from pressures cores from Lee & Collett (2009).

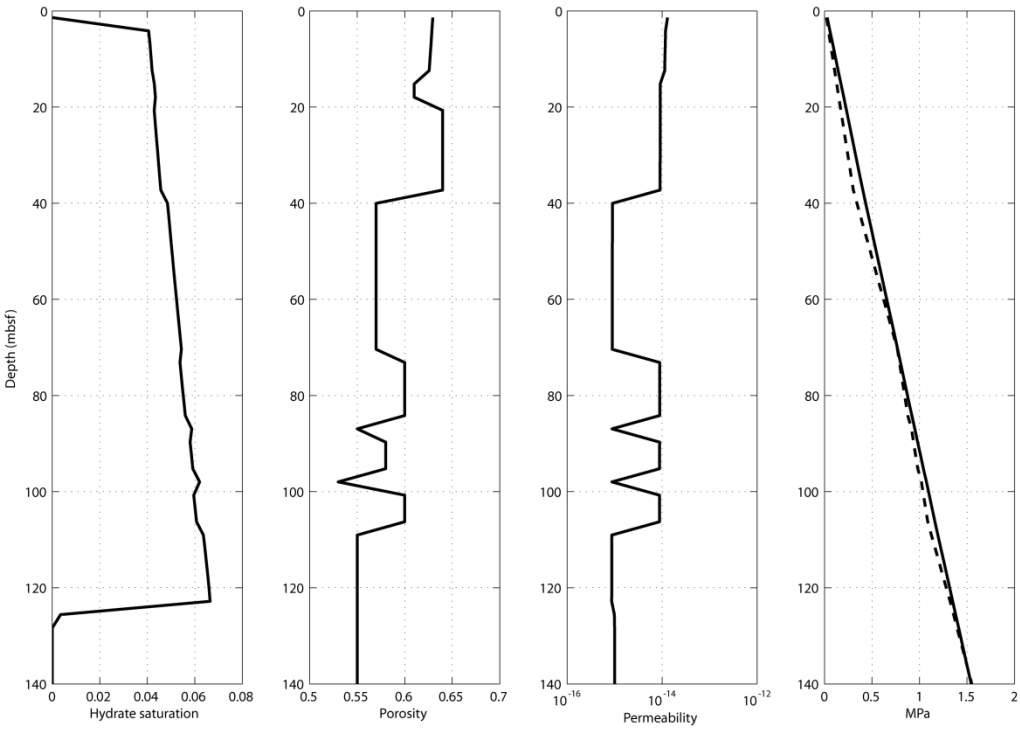

Figure 5. Model results for Hydrate Ridge with heterogeneous porosity and permeability profiles. Vertical flow rate is 300 mm yr^{-1}, and fractures occur after 970 years near 70 mbsf at the base of a low-permeability layer.

Subtask 8.3: Integrating geomechanical studies

This task has essentially been incorporated in Subtask 8.2 as we use geomechanical field data to test our stability and fracture models.

References

Bhatnagar, G., Chapman, W.G., Dickens, G.R., Dugan, B., Hirasaki, G.J., 2007. Generalization of gas hydrate distribution and saturation in marine sediments by scaling of thermodynamic and transport processes. *Am. J. Sci.,* 307, 861-900, doi:10.2475/06.2007.01.

Davie, M.K., Buffett, B.A., 2001. A numerical model for the formation of gas hydrate below the seafloor. *J. Geophys. Res.,* 106(B1), 497-514.

Egeberg, P.K., Dickens, G.R., 1999. Thermodynamic and pore water halogen constraints on gas hydrate distribution at ODP Site 997 (Blake Ridge). *Chem. Geol.*, 153, 53-79.

Finkbeiner, T., Zoback, M., Flemings, P., Stump, B., 2001. Stress, pore pressure, and dynamically constrained hydrocarbon columns in the South Eugene Island 330 field, northern Gulf of Mexico. *AAPG Bull.,* 85(6), 1007-1031.

Lee., M.W., Collett, T.S., 2009. Gas hydrate saturations estimated from fractured reservoir at Site NGHP-01-10, Krishna-Godavari Basin, India. *J. Geophys. Res.*, 114, B07102, doi:10.1029/2008JB006237.

Lee, M.W., Collett, T.S., 2006. Gas hydrate and free gas saturations estimated from velocity logs on Hydrate Ridge, offshore Oregon, USA. In Tréhu, A.M., Bohrmann, G., Torres, M.E., Colwell, F.S., (Eds.) *Proc. ODP, Sci. Results*, 204, Ocean Drilling Program, College Station, TX, doi:10.2973/odp.proc.sr.204.103.2006.

Rempel, A.W., 2007. Formation of ice lenses and frost heave. *J. Geophys. Res.,* 112, F02S21, doi:10.1029/2006JF000525.

Sloan, E.D. Jr., 1990. *Clathrate Hydrates of Natural Gases*. M. Dekker, New York, 641 pp.

Torres, M.E., McManus, J., Hammond, D.E., de Angelis, M.A., Heeschen, K.E., Colbert, S.L., Tryon, M.D., Brown, K.M., Suess, E., 2002. Fluid and chemical fluxes in and out of sediments hosting methane hydrate deposits on Hydrate Ridge, OR, I: Hydrological provinces. *Earth Planet. Sci. Lett.*, 201, 525-540.

Weinberger, J.L., Brown, K.M., 2006. Fracture networks and hydrate distribution at Hydrate Ridge, Oregon. *Earth Planet. Sci. Lett*., 245, 123-136, doi:10.1016/j.epsl.2006.03.012.

Task 9: Geophysical Imaging of Gas Hydrate and Free Gas Accumulations
P. Jaiswal and C.A. Zelt

Summary
We primarily focused on generating velocity model and reflectivity image using the seismic line offshore Krishna-Godavari basin, East coast India. We have completed Subtask 9.1 by developing low-frequency velocity model and a corresponding depth image using the Unified Imaging approach (Jaiswal and Zelt, 2009). We started with 2-D waveform inversion but had to put the work on hold from September 2009 due to Priyank's appointment at Oklahoma State University, Stillwater. Priyank is currently setting up a geophysical computational lab with same specifications as at Rice University. We have also started working on Subtask 9.3 (rock-physics modeling).

Milestone Status
9.1 Preliminary processing and inversion of seismic data– completed, manuscript under preparation.
9.2 Final 1-D elastic and 2-D acoustic waveform inversion – ongoing but delayed due to development of lab at Oklahoma State University.
9.3 Rock physics modeling – this is ongoing work and will be completed on target. Hydrates appear to be pore-filling at the end of the model that has been experiencing high sedimentation while they are present in fracture network at the sediment starved end of the model. We assume that existing modeling methods would suffice our needs for this but may have to look for an improved way of modeling hydrates in fractured network. We will be looking for collaboration opportunities with Stanford in near future.

Subtask 9.1: Preliminary Processing and Inversion
This task has been completed. The manuscript is in preparation. However a few figure are presented to recapitulate the work.

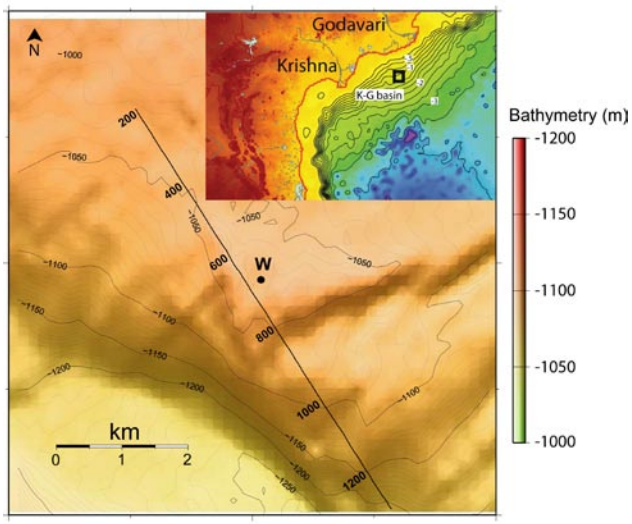

Figure 1. Basemap. Seismic line is indicated in black line with CDPs labeled in multiples of 200. Location of the Well W is indicated in solid dot. Bathymetry is labeled every 50m. Location of the study area with respect to India is shown in inset with rivers Krishna and Godavari labeled. Bathymetry is labeled in km.

Arrival times from five geological interfaces, including the seafloor and the bottom simulating reflector (BSR) were inverted to obtain the final traveltime model (Figure 2) and a corresponding stack (Figure 3). The data were pre-stack depth migrated using the traveltime model and a depth image (Figure 4) was obtained. A feature relevant to understanding the gas-hydrate distribution along the seismic line appears to be a mound between CMPs 450-700 (Figures 3 and 4). The BSR appears to have diminished reflectivity below the mound. The mound appears to be bounded by normal faults on both sides. The mound appears to have divided the region in two parts: to the SE of the mound the velocity distribution is patchy and in NW side of the mound velocities appear to the more uniformly distributed. Also, SE of the mound appears to contain more discontinuous and patchy reflections compared to the NW side.

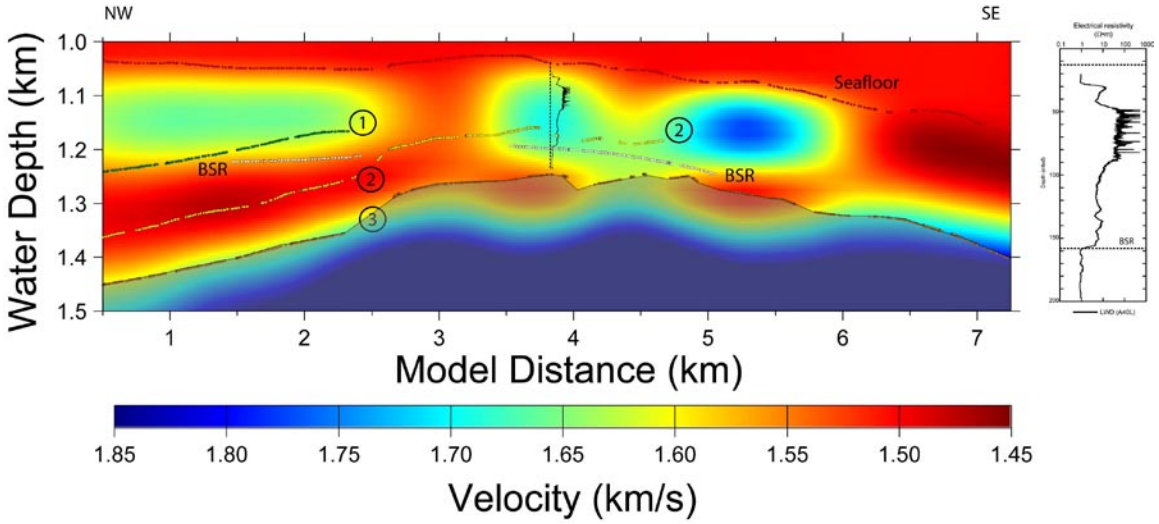

Figure 2. Velocity Model. Seafloor and BSR along with three horizons (1, 2, and 3) that are used for traveltime inversion are labeled. The sediment velocity above horizon three seems to be ~1.5 km/s. Regions of enhanced velocity above BSR suggest presence of hydrates. P-wave log is overlaid at the appropriate location. Parts of the model not covered by reflections are masked.

The thickness of the strata between the orange and the green horizons (Figure 3 and 4) NW of the mound is the same as thickness between orange horizon and the seafloor SE of the mound. This implies that a) seafloor SE of the mound is roughly equivalent to the green horizon NW of the mound, and b) NW part of the mound has experienced sedimentation while SE of the mound remained sediment starved. The mound may be acting as a sediment barrier. The expanding sediment thickness towards NW and onlaps (Figure 3) further suggests that the sedimentation is syn-tectonic. Sediment accumulation NW of the mound lead to the possibility of more hydrates being formed as compared to SE. This raises an immediate question – why does SE of mound has higher velocity?

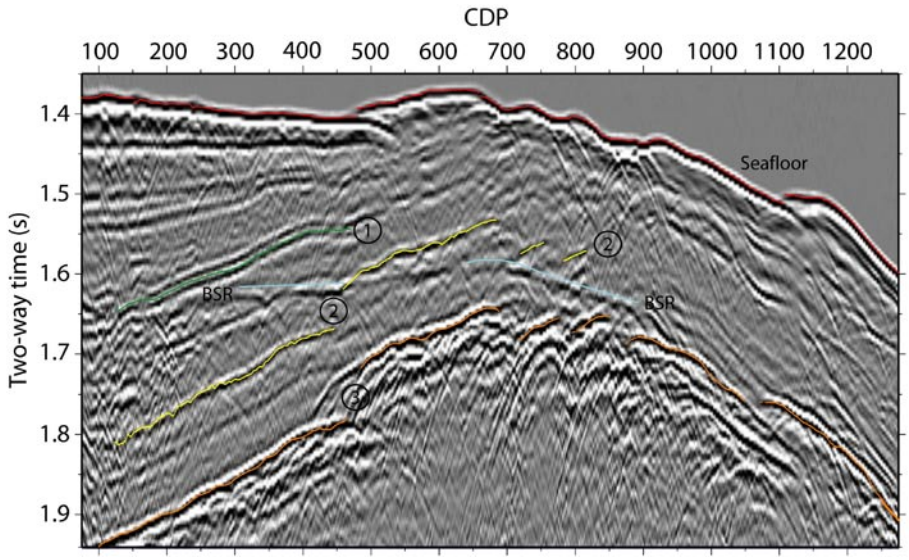

Figure 3. Stack data. Seafloor and BSR along with three horizons (1, 2, and 3) that are used for traveltime inversion are labeled.

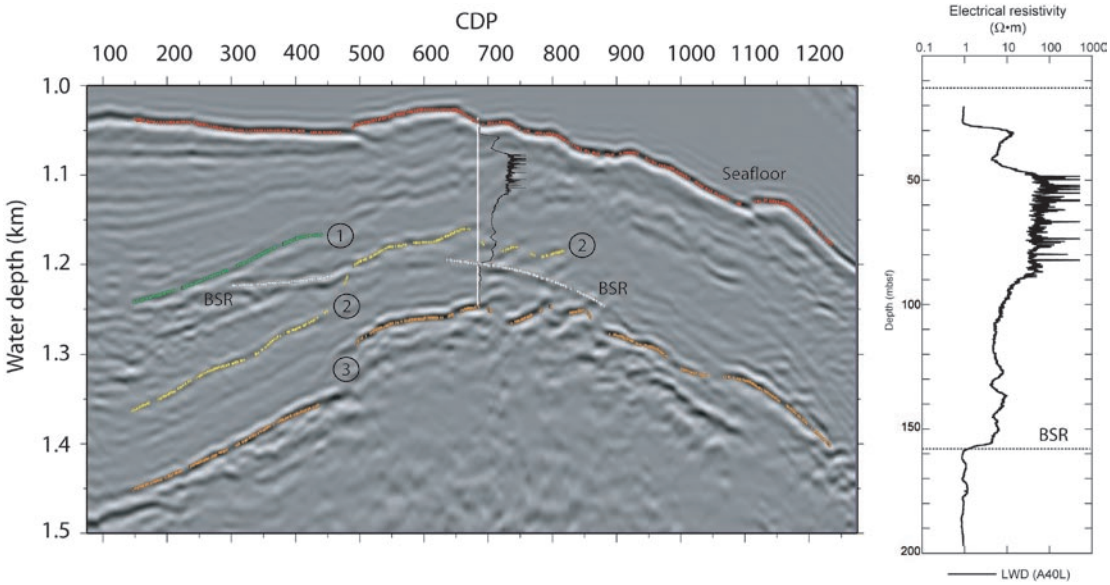

Figure 4. Pre-Stack depth migrated image. Seafloor and BSR along with three horizons (1, 2, and 3) that are used for traveltime inversion are labeled. Trajectory of W (Figure 1) is indicated with a solid white line. Also displayed is the resitivity log along the trajectory. Note the BSR in the log well coincides with the BSR in the migrated image.

Subtask 9.3: ***Rock physics modeling using the low frequency model***

The high velocity zones SE of the mound appears to be coinciding with incoherent (lacking identifiable horizon) zones of reflectivity intermittent with zones of coherent reflectivity (Figures 3 and 4). SE of the mound also appears to be having more faults and fractures (more diffractions in the stack). NW of the mound appears to be lacking faults and fractures in general, has continuous

interpretable reflection events, and a homogenous spread in velocity. We speculate that the hydrates are present in different styles in either side of the mound; while hydrates are present as pore-fills NW of mound, they are present as load bearing matrix-component SE of the mound.

The main aim of using rock physics is to be able to model the variations in the elastic moduli of the rock which essentially is being able to predict *Vp* and *Vs* variations. We are driven by Effective Medium Modeling by Dvorkin et al. (1999).

Effective Medium Modeling: This model assumes that the rock moduli lies between the moduli of dry sediment at the critical porosity and the point of zero rigidity (Figure 6). The moduli for the intermediate porosity are calculated using upper Hashin Shtrikman bound. The fluid-saturated bulk and shear moduli are calculated using Gassmann's equation. The main assumption of this model is that the modulus-pressure behavior of high porosity sediment is similar to that of a dense random pack of identical elastic spheres. The porosity of this pack is 36 - 40% which is called critical porosity. In this model the input parameters are differential pressure, porosity, and mineralogy of the sediment.

First, modeling for the elastic moduli of the dry sediment frame is done. For the unconsolidated rock matrix whose porosity is below critical φ_c (φ_c = 36 - 40%) effective medium model connects two end points in the modulus-porosity plane, one at zero porosity where the rock's elastic moduli are those of the solid phase and the other at the critical porosity where sediment is modeled as random pack of identical spheres.

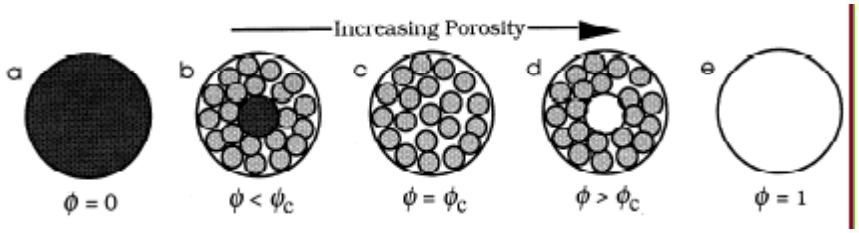

Figure 6. Hashin-Shtrikman arrangements of sphere pack, solid, and void. From left to right: pure solid at zero porosity; pure solid enveloped by the sphere pack phase; sphere pack at critical porosity; void enveloped by sphere pack phase; and void at 100% porosity.

At porosity $\varphi < \varphi_c$ the concentration of the pure solid phase in the rock is $(1 - \varphi) / \varphi_c$ and that of the sphere pack phase is φ / φ_c. The dry frame bulk moduli K_{dry} and shear moduli G_{dry} can be expressed as:

$$K_{Dry} = \left[\frac{\phi/\phi_c}{K_{HM} + \frac{4}{3}G_{HM}} + \frac{1-\phi/\phi_C}{K+} \right]^{-1} - \frac{4}{3}G_{HM};$$

$$G_{Dry} = \left[\frac{\phi/\phi_c}{G_{HM}+Z} + \frac{1-\phi/\phi_c}{G+Z} \right]^{-1} - Z; Z = \frac{G_{HM}}{6}\left(\frac{9K_{Hm}+8G_{HM}}{K_{HM}+2G_{HM}} \right)$$

Where

$$K_{HM} = \left[\frac{n^2(1-\phi_c)^2 G^2}{18\pi^2(1-\nu)^2} P \right]^{\frac{1}{3}}, G_{HM} = \frac{5-4\nu}{5(2-\nu)} \left[\frac{3n^2(1-\phi_c)^2 G^2}{2\pi^2(1-\nu)^2} P \right]^{\frac{1}{3}}$$

K_{HM} and G_{HM} are elastic moduli at critical porosity.

Where ϕ_c is the critical porosity (ϕ_c=0.3-0.4; Nur et,al., 1998); and G and ν are the shear modulus and Poisson's ratio of the solid phase respectively. ν is related to G and K (the solid phase, modulus) by:

$$\nu = 0.5(K - \tfrac{4}{3}G)/(K + \tfrac{1}{3}G).$$

P is the differential pressure; *K*, *G,* and ν are the bulk and shear moduli of the solid phase, and its Poisson's ratio, respectively; *n* is the average number of contacts per grain in the sphere pack. This number is between 7 and 9 (Mavko et al., 1998).The differential pressure is the difference between the lithostatic and hydrostatic pressures:

$$P = (\rho b - \rho w) g D,$$

Where ρ_b is the bulk density of the sediment; ρ_w is water density; *g* is the gravity acceleration; and *D* is depth below sea floor.

At porosity $\varphi > \varphi_c$, the concentration of the void phase is $(\varphi - \varphi_c) / (1 - \varphi_c)$ and that of the sphere-pack phase is $(1 - \phi_c) / (1 - \phi_c)$. For porosity that is larger than the porosity of the sphere pack, the dry frame bulk moduli K_{dry} and shear moduli G_{dry} are given by the following formula.

$$K_{Dry} = \left[\frac{(1-\phi)/(1-\phi_c)}{K_{HM} + \frac{4}{3}G_{HM}} + \frac{(\phi-\phi_c)/(1-\phi_c)}{\frac{4}{3}G_{HM}} \right]^{-1} - \frac{4}{3}G_{HM},$$

$$G_{Dry} = \left[\frac{(1-\phi)/(1-\phi_c)}{G+Z} + \frac{(\phi-\phi_c)/(1-\phi_c)}{Z} \right]^{-1} - Z$$

Dry frame moduli calculation from measured P-wave velocity and that calculated using Gassmann's equation give the shear wave velocity. For sediments saturated with pore fluid of bulk modulus K_f, the bulk modulus K_{Sat} is calculated using Gassmann's equation (1951) as:

$$K_{Sat} = K\frac{\phi K_{Dry} - (1-\phi)K_f K_{Dry}/K + K_f}{(1-\phi)K_f + \phi K - K_f K_{Dry}/K}, G_{Sat} = G_{Dry}$$

The elastic wave velocity is then given by:

$$V_P = \sqrt{\left(K_{Sat} + \frac{4}{3}G_{Sat}\right)/\rho_B},$$
$$V_S = \sqrt{G_{Sat}/\rho_B}$$

Where ρ_b is the bulk density. The porosity in the model is the total porosity of the sediments.

To calculate elastic modulus for a composite of minerals we have used Hill's formula (Hill 1952):

$$K = \frac{1}{2}\left[\sum_{i=1}^{m} f_i k_i + \left(\sum_{i=1}^{m} f_i/k_i\right)^{-1}\right], G = \frac{1}{2}\left[\sum_{i=1}^{m} f_i G_i + \left(\sum_{i=1}^{m} f_i/G_i\right)^{-1}\right]$$

Where m is the number of mineral constituents; f_i is the volumetric fraction of the i –th constituent in the solid phase; and K_i and G_i are the bulk and shear moduli of the i – th constituent, respectively

For the well (W; Figure 1), to calculate the bulk and shear modulus of saturated sediment we have followed the following procedure. First of all the effective bulk (K_{HM}) and shear (G_{HM}) moduli of the pack (dry) is given by Hertz-Mindlin (Mindlin, 1949) contact theory, calculated assuming 100% Clay for KG-Basin. n=9 is the average number of contacts per grain in the sphere pack. The differential pressure P (MPa), geothermal gradient (^{0}C/Km) and seafloor temperature T (^{0}C) are obtained from the initial report data that are used to calculate the pressure and temperature all along the log interval below the seafloor.

The critical porosity is determined by using the suggested values (Mavko et al. 1998). To get the critical porosity in KG-Basin we have considered other sites that are hydrate free (4A and 6A; Shipboard Expedition 2007). We plotted porosity vs P-wave velocity, the critical porosity value we obtained from these two sites ranges from ϕ_c=0.62 to 0.65.

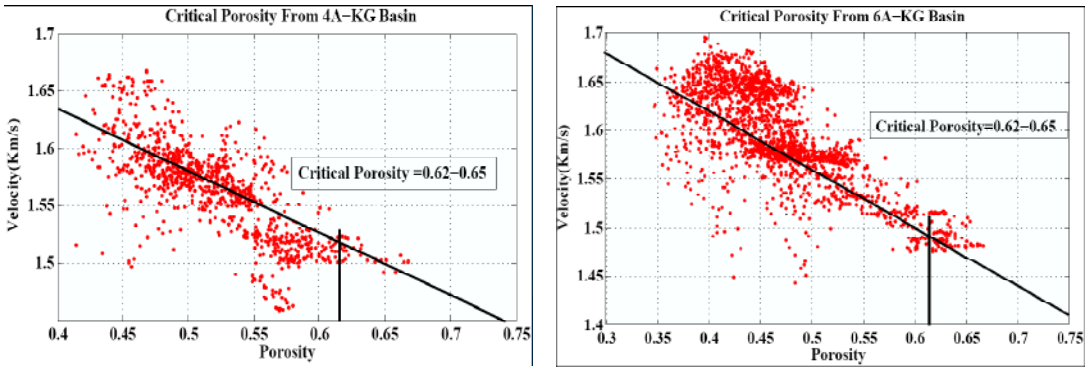

Figure 7. Critical porosity from hydrate-free sites in the K-G basin.

The dry rock bulk (K_{Dry}) and shear (G_{Dry}) are first calculated following which the saturated sediment bulk (K_{Sat}) and shear (G_{Sat}) modulus are calculated using Gassmann's equation. The P-wave (V_P) and S-wave (V_S) velocities are finally calculated. We apply the theory to reproducing P-wave velocity data from well W (Figure 1).

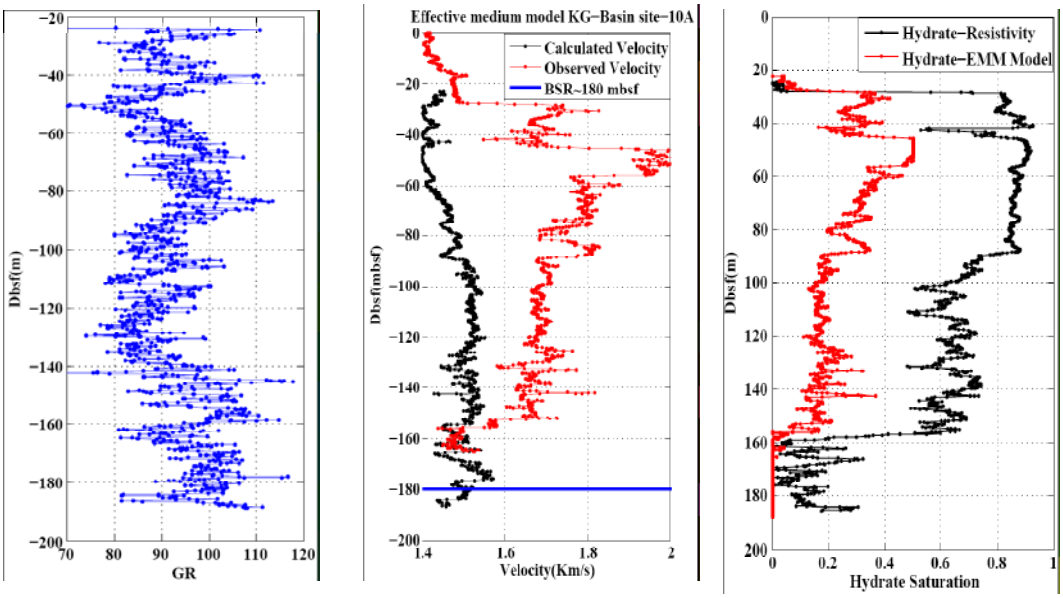

Figure 8. Modeling for W. left: Gamma ray log. Center: Observed (sonic log) vs calculated P-wave velocity. The observed velocities may be higher as they are calculated using sonic frequencies. Right: Calculated saturation from resistivity log versus from rock physics modeling.

For NW of the mound we use Gassman's equation and assume that hydrates are in pore-spaces. For SE of the mound we assume that hydrates are

present as a component of the rock matrix and model the elastic constants using Hill's formula. The final concentrations are illustrated in Figure 9.

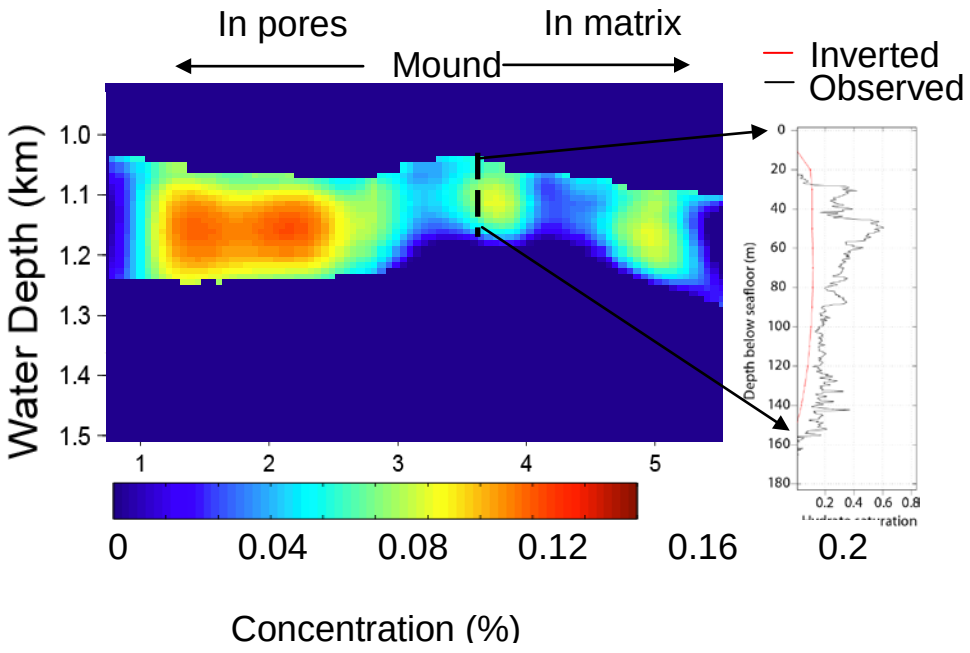

Figure 9. NW of the model has higher hydrate concentration but lower velocity. SE of the mound has lower concentration but higher velocity. Most likely, this is due to hydrates being present in different states (pore-fills in the NW and matrix component in the SE).

References:

Dvorkin, J., M. Prasad, A. Sakai, and D. Lavoie, 1999, Elasticity of marine sediments: Rock physics modeling, Geophys. Res. Lett., 26(12), 1781–1784.

Gassman, F., Elastic Waves Through A Packing Of Spheres, 1951, Geophysics 16, 673, DOI:10.1190/1.1437718

Hill, R., The Elastic Behaviour of a Crystalline Aggregate, 1952, Proc. Phys. Soc., 65, 349-354, 10.1088/0370-1298/65/5/307

Jaiswal, P., and C.A. Zelt, 2008, Unified Imaging of Multichannel Seismic Data: Combining Traveltime Inversion and Pre-Stack Depth Migration, *Geophysics,* 73, DOI:10.1190/1.2957761.

Mavko, G., T. Mukherjee, and J. Dvorkin, 1998, Rock Physics Handbook, Cambridge University Press, Cambridge

Mindlin, RD, Compliance of elastic bodies in contact, 1949, J. Appl. Mech., 16, 259–268

Nur, A., G. Mavko, J. Dvorkin, and D. Galmudi, 1998, Critical porosity: a key to relating physical properties to porosity in rocks, The Leading Edge, 17, 357-362

Presentations and Manuscripts:

Jaiswal P., Zelt, C.A., and Dewangan, P., Gas-Hydrates in the Krishna-Godavari Basin, International Lithosphere Program (ILP) 2009 meeting, Clermont-Ferrand, October 5-9, 2009

Dewangan, P., Gullapallis, S., and Jaiswal, P., Hydrates distribution in the Krishna-Godavari basin from concurrent seismic profiles, *manuscript in preparation.*

Task 10 Technology Transfer

The team participated in a research review teleconference with NETL on June 30, 2009. Except for during the summer, the research team has monthly seminar/coordination meetings.

Publications

J. Phirani, R. Pitchumani, , and K. K. Mohanty, “Transport Properties of Hydrate Bearing Formations from Pore-Scale Modeling,” SPE 124882, paper prepared for presentation at the 2009 SPE Annual Technical Conference and Exhibition held in New Orleans, Louisiana, USA, 4–7 October 2009.

J. Phirani, K. K. Mohanty, and G. J. Hirasaki, “Warm Water Flooding of Unconfined Gas Hydrate Reservoirs,” Energy Fuels XXXX, XXX, 000–000 : DOI:10.1021/ef900291j

DOE Grants R15620, RO15621, RO15622 **9/30/2009**

Phase 4

"Detection and Production of Methane Hydrates"

COST PLAN / STATUS									
	Phase 1	**Phase 2**	**Phase 3**	**Phase 4 7/01/09 - 6/30/10**				**Phase 4**	
Baseline Quarter Reporting	10/06-6/07	7/07-6/08	7/08-6/09	7/1/09 - 9/30/09	10/1/09 - 12/31/09	1/1/10 - 3/31/10	4/1/10 - 6/30/10	Totals	Cumulative Totals
Baseline Cost Plan Allocation (SF- 424A)									
Federal Share	$ 3,624	$320,010	$ 331,135	$ 89,012	$ 89,012	$ 89,012	$ 89,012	$ 356,048	$ 1,010,817
Non-Federal Share	$ 1,004	$114,613	$ 107,630	$ 27,622	$ 27,622	$ 27,622	$ 27,622	$ 110,488	$ 333,735
Total Planned	$ 4,628	$434,623	$ 438,765	$ 116,634	$ 116,634	$ 116,634	$ 116,634	$ 466,536	$ 1,344,552
Cumulative Baseline Cost	$ 4,628	$439,251	$ 878,016	$ 116,634	$ 116,634	$ 116,634	$ 116,634	$ 466,536	$ 1,344,552
Actual Incurred Cost									
Federal Share	$ 3,082	$298,506	$ 242,993	$ 74,631				$ 74,631	$ 619,212
Non-Federal Share	$ 1,091	$118,145	$ 95,520	$ 5,078				$ 5,078	$ 219,834
Total Incurred	$ 4,173	$416,651	$ 338,513	$ 79,709				$ 79,709	$ 839,046
Cumulative Costs	$ 4,173	$420,824	$ 759,337	$ 79,709				$ 79,709	$ 839,046
Variance (plan-actual)									
Federal Share	$ 542	$ 21,504	$ 88,142	$ 14,381				$ 14,381	$ 124,569
Non-Federal Share	$ (87)	$ (3,533)	$ 12,110	$ 22,544				$ 22,544	$ 31,034
Total Variance	$ 455	$ 17,971	$ 100,252	$ 36,925				$ 36,925	$ 155,603
Cumulative Variance	$ 455	$ 18,426	$ 118,678	$ 155,603				$ 155,603	$ 155,603

Milestone Plan/Status

Task	Milestone: Status and Results	Date	Status
5. Carbon inputs and outputs to gas hydrate systems	5.1a Measure iodine in sediments We have measured iodine concentrations in pore waters and sediments from 4 gas hydrate systems.	12/07	Done (except writing)
	5.1b Constrain C_{org} inputs from iodine We have measured the content and isotopic composition of organic carbon and carbonate in sediment from cores of several gas hydrate systems. We are beginning to incorporate the results into models.	10/08	Partly Done
	5.2a Construct metal profiles in sediments We have measured metal contents in pore water and sediment from cores of two gas hydrate systems along the Peru Margin and in the Sea of Japan. The Sea of Japan work has been published (Snyder et al., 2007).	12/09	Done (except writing)
	5.2b Modeling/integrating profiles We are beginning to incorporate the results into models. We have written an article defending our use of the SMT as a proxy for methane loss through AOM.	12/10	Begun

6. Numerical models for quantification of hydrate and free gas accumulations	6.1 Model development. The recipient shall develop finite difference models for the accumulation of gas hydrate and free gas in natural sediment sequences on geologically relevant time scales.	9/07	done

	6.2: Conditions for existence of gas hydrate The recipient shall summarize, quantitatively, the conditions for the absence, presence, and distribution of gas hydrates and free gas in 1-D systems by expressing the conditions in terms of dimensionless groups that combine thermodynamic, biological and lithologic transformation, and transport parameters.	3/07	done
	6.3 Compositional effect on BSR The recipient shall add to the numerical model, developed under this task, a chloride balance and multi-hydrocarbon capability specifically to investigate how hydrocarbon fractionation might affect Bottom Simulating Reflectors (BSRs).	7/07	In Progress
	6.4: Amplitude Attenuation and chaotic zones due to hydrate distribution The recipient shall simulate preferential formation of gas hydrate in coarse-grained, porous sediment in 2-D by linking fluid flux to the permeability distribution.	3/09	started
	6.5: Processes leading to overpressure The recipient shall quantify, by simulation and summarize by combination of responsible dimensionless groups, the conditions leading to overpressure to the point of sediment failure.	3/08	Collaborating with task 8
	6.6 Concentrated hydrate and free gas The recipient shall, using 2-D and 3-D models, simulate lateral migration and concentration of gas hydrate and free gas in structural and stratigraphic traps.	3/08	ongoing
	6.7 Focused free gas, heat and salinity The recipient shall quantify, using 2-D and 3-D model simulations and comparisons to available observations, the factors controlling the process of localized upward migration of free gas along faults and lateral transfer to dipping strata that can lead to chaotic zones and possible accumulations of concentrated hydrate.	9/09	started

	6.8 Sulfate profile as indicator of methane flux The recipient shall compute, for systems where data on the sulfate profile is available, the oxidation of methane by sulfate and shall indicate the perceived level of effect on gas hydrate accumulation and the data's value as an indicator of methane flux.	7/07	Revisited to collaborate with Task 5.
	6.9 Application of models to interpretation of case studies. The models developed in Task 6 will be applied to case studies in the interpretation of each of the other tasks.	6/10	started
7. Analysis of production strategy	7.1a Pore scale model development and Hydrate code comparison For this milestone, we will develop pore-scale models of hydrate accumulation by simulation. Our hydrate code will be used to solve a set of problems formulated by the Code Comparison Study group. Our results will be compared with those of other hydrate codes. Should be changed to: 6/08 Reason: The starting date was moved to 6/07 Status: Code comparison study is 80% complete.	1/08	6/08 Code comparison is done.
	7.1b Petrophysical and thermophysical properties of hydrate sediments from pore-scale model For this milestone, we will assume the pore-scale models of hydrate accumulation developed in the last milestone and estimate transport properties as a function of hydrate and gas saturations. Should be changed to: 6/09 Reason: The starting date was moved to 6/07 Status: Have not started	1/09	In progress
	7.2a Modeling of several production strategies to recover gas from marine hydrates Several production strategies would be modelled using the transport property correlations developed in the previous milestone. Optimal strategies will be identified.	1/10	In progress

	Should be changed to: 6/10		
	7.2b Effect of marine reservoir heterogeneities on production of methane Reservoir heterogeneity anticipated in marine environments (known or determined through other tasks) would be incorporated. Appropriate hydrate distributions, either constrained from experimental data or mechanistic simulations (Task 5) would be used. Sensitivity of gas production to the heterogeneities would be calculated. Should be changed to: 6/11 Reason: The starting date was moved to 6/07 Status: Have not started	12/10	6/10
8. Seafloor and borehole stability	8.1a Collection of data We have collected the published data and are working it into a data base. We are also working on a review paper summarizing the state of the art settings. This will include laboratory experiments, field data, published results, and unpublished data.	05/08	Completed
	8.1c Complete database We are organizing the data from task 8.1a into a format that can be searched and used by researchers trying to understand mechanical behavior of hydrate-bearing sediment. We will also identify key gaps in the database for focusing future hydrate research endeavors. We have started exchanging these data with the modeling components of this project.	10/09	On target
	8.2a Link database with models We have started passing data along to the modeling groups so they can use sediment properties from hydrate provinces as they simulate hydrate accumulation and production.	08/08	On target
	8.2b Add sediment stability to models Standard stability calculations have been implemented in a standard basin model. Now that it is functional we will work with the hydrate accumulation model to add a stability	10/08	On target

	calculation to the 2-D models.		
	8.2c Conditions for (in)stability After implementing the stability model in the hydrate accumulation code, we can explore the conditions (e.g., hydrate dissociation, sea-level fall) that could drive slope failure and hydrate/methane release or lead to borehole failures during production.	9/09	On target
9 Geophysical imaging of hydrate and free gas	9.1 Preliminary processing and inversion of seismic data. Perform conventional seismic reflection processing, velocity analysis, travel time tomography, and other analyses as deemed appropriate and necessary.	8/08	Done
	9.2: Final 1-D elastic and 2-D acoustic waveform inversion. Apply 1-D elastic and 2D acoustic inversions on data obtained from subtask 9.1 to derive determine high-resolution elastic and acoustic properties.	8/09	Delayed due to lab development
	9.3: Rock physics modeling. Apply rock physics models to the developed seismic models to estimate hydrate saturation and lithology through application of well log data in conjunction with data from subtask 9.2. For this subtask we shall seek to collaborate with research being conducted under separately funded DOE-NETL projects (DE-FC26-05NT42663 with Stanford University, "Seismic-Scale Rock Physics of Methane Hydrate" and others as applicable).	8/10	On Target

National Energy Technology Laboratory

626 Cochrans Mill Road
P.O. Box 10940
Pittsburgh, PA 15236-0940

3610 Collins Ferry Road
P.O. Box 880
Morgantown, WV 26507-0880

One West Third Street, Suite 1400
Tulsa, OK 74103-3519

1450 Queen Avenue SW
Albany, OR 97321-2198

539 Duckering Bldg./UAF Campus
P.O. Box 750172
Fairbanks, AK 99775-0172

Visit the NETL website at:
www.netl.doe.gov

Customer Service:
1-800-553-7681